

Chemical and radiative transfer modeling of Propylene Oxide

Ankan Das^{1,*}, Prasanta Gorai¹ and Sandip K. Chakrabarti¹

Indian Centre for Space Physics, 43 Chalanika, Garia Station Road, Kolkata 700084, India

e-mail: ankan.das@gmail.com

June 14, 2019

ABSTRACT

Context. The recent identification of the first complex chiral molecule, propylene oxide (PrO) in space opens up a new window to further study the origin of homochirality on the Earth. There are some recent studies to explain the formation of PrO however additional studies on the formation of this species are needed for better understanding.

Aims. We seek to prepare a complete reaction network to study the formation of propylene oxide in the astrophysically relevant conditions. Based on our results, a detailed radiative transfer modeling has been carried out to propose some more transitions which would potentially be targeted in the millimeter wave domain.

Methods. Gas-grain chemical network was used to explain the observed abundance of PrO in a cold shell surrounding the high-mass star-forming region of Sgr B2. Quantum chemical calculations were employed to study various reaction parameters and to compute multiple vibrational frequencies of PrO.

Results. To model the formation of PrO in the observed region, we considered a dark cloud model. Additionally, we used a model to check the feasibility of forming PrO in the hot core region. Some potential transitions in the millimeter wave domain are predicted which could be useful for the future astronomical detection. Radiative transfer modeling has been utilized to extract the physical condition which might be useful to know the properties of the source in detail. Moreover, vibrational transitions of PrO has been provided which could be very useful for the future detection of PrO by the upcoming James Webb Space Telescope (JWST).

Key words. Astrochemistry–ISM: molecules–ISM: abundances–ISM: evolution–Method: numerical

* ankan.das@gmail.com

1. Introduction

The discovery of a large number of complex interstellar species significantly improved our understanding of the chemical processes involved in the Interstellar Medium (ISM). It is speculated that the building blocks of life (biomolecules) were formed in the ISM and were delivered by the comets to the Earth in the later stages (Chyba et al. 1990; Raymond et al. 2004; Hartogh et al. 2011). The life making primordial organic compounds may also have been formed in the pre-solar nebula rather than on the early Earth (Bailey et al. 1998; Chakrabarti & Chakrabarti 2000a,b; Hunt-Cunningham & Jones 2004; Holtom et al. 2005; Buse et al. 2006; Herbst & van Dishoeck 2009). The prospect of extra-terrestrial origin of biomolecules is a fascinating topic since many biomolecules are chiral. Synthesis and detection of prebiotic molecules in the ISM have been studied and discussed by various authors (Cunningham et al. 2007; Das et al. 2008a; Gupta et al. 2011; Majumdar et al. 2012; Garrod, R.T 2006; Nuevo et al. 2014; Chakrabarti et al. 2015). In between the living organisms on the Earth, amino acids and sugars are chiral. Interestingly, most of the amino acids of terrestrial proteins and sugars found on the earth are homochiral; Amino acids are left-handed whereas sugars are right-handed. When and how this homochirality developed on the Earth is a matter of debate (Cohen et al. 1995). In the Murchison meteorite, various bio-molecules were identified. Interestingly, an excess amount of L-amino acids were identified (Engel & Nagy 1982; Engel & Macko 1997) which also suggest an extraterrestrial source for molecular asymmetry in the Solar System. Thus, observation of more chiral species along with their enantiomeric excess in space could be very useful for the better understanding of the origin of homochirality. But unfortunately, with the present observational facility, it is quite difficult to define the enantiomeric excess of an interstellar species.

Cunningham et al. (2007) attempted to observe PrO in the Orion KL and Sgr B2(LMH) by using the Mopra Telescope. Based on their observational results, they predicted an upper limit on the column density ($\sim 6.7 \times 10^{14} \text{ cm}^{-2}$) of PrO in the Sgr B2 (LMH) and predicted an excitation temperature of 200 K with a compact source size of $5''$. Recently, McGuire et al. (2016) attempted to search for the existence of the complex chiral species in space. They targeted the star-forming region like, Sgr B2 with Parkes and Green Bank Telescope (GBT) and successfully identified the first complex chiral molecule (PrO) in space. They were unable to determine the enantiomeric excess of PrO due to the lack of high precision and full polarization state measurement. McGuire et al. (2016) identified three transitions of PrO in absorption which correspond to the excitation temperature of $\sim 5 \text{ K}$, and column density $\sim 1 \times 10^{13} \text{ cm}^{-2}$.

PrO has a significant proton affinity (Hunter & Lias 1998) and should be converted into protonated form through some ion-neutral reactions. Figure 1abc depict the structure of PrO and its two protonated form respectively. Swalen & Hershbach (1957) and Hershbach & Swalen (1958) discussed the internal barrier of PrO and its various rotational transitions in the ground and torsionally excited states. Later, Creswell & Schwendeman (1977) calculated the centrifugal distortional constants and structural parameters of PrO. The absorption spectrum of PrO was studied by various

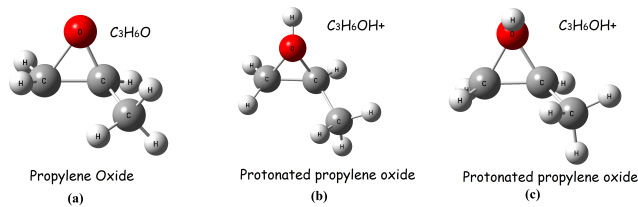


Fig. 1. Structure of propylene oxide and two of its protonated form.

authors (Polavarapu et al. 1985; Lowe et al., 1986; Gontrani et al. 2014). Recently, the IR spectrum of solid PrO was experimentally obtained by Hudson et al. (2017). They also proposed that the reaction between O atom and C_3H_6 may lead to the formation of PrO and its four other isomers. We have considered these pathways in our model to study the formation of PrO and its isomers.

A Large number of observational and theoretical studies reveal that the complex organic molecules (COMs) begin to form in the cold region of the dense molecular cloud. Cosmic dust particles act as a reservoir for molecules and also as a catalyst for reactions, which lead to the formation of COMs in molecular clouds (Öberg et al. 2009; Bacmann et al. 2012; Das et al. 2016). In low temperature and moderately high-density regions, gas phase exothermic reactions (such as ion-neutral reactions) are more feasible because they do not possess any activation barrier (Agúndez & Wakelam 2013). At the same time, various irradiation-triggered solid-phase reactions also contribute to the formation of various complex interstellar species. In the low temperature, non-thermal desorption mechanism plays an efficient means to transport the surface species into the gas phase upon its formation. In this process, all the surface reactions which are exothermic and resulting in a single product can break the surface-molecule bond with some fraction and transfer the surface species to the gas phase (Garrod, Wakelam & Herbst 2007). Non-thermal reactions on the grain surface also play a crucial role in governing the abundances of the surface species where the diffusion of atom (ground state) or radical diffusion chemistry is inefficient. Oxygen(1D) insertion reaction mentioned in Bergner et al. (2017); Bergantini et al. (2018) can be characterized as the non-thermal reactions. These excited oxygens or supra-thermal oxygens(1D) are mainly produced by the effects of secondary electrons generated in the path of cosmic rays when it is in contact with the grain mantle. Main source of these oxygens are the various oxygen rich species like, CO_2 , H_2O and CO .

Occhiogrosso et al. (2012) carried out theoretical modeling for the formation of Ethylene Oxide (EO) in space. They were able to reproduce the observed abundance of EO successfully. Additionally, they considered the reaction between C_3H_6 and O on the surface to include the formation of PrO. However, they did not include a complete reaction network for the creation and destruction of PrO and its associated species. More importantly, they did not consider the formation of C_3H_6 on grain surface. Recently Hickson et al. (2016) provided some pathways for the formation of C_3H_6 on the grain surface which eventually can produce PrO.

In this paper, we study the synthesis of PrO along with two of its structural isomers, namely, propanal and acetone in star-forming conditions. The radiative transfer models have been carried out to identify the most active transition of PrO in the millimeter(mm) wave regions. Absorption

Table 1. Surface Reactions For Propylene and Propylene Oxide Synthesis.

Reaction number(type)	Reaction	E_a in Kelvin
R1(NR) ^a	$H + C_3 \rightarrow 1 - C_3H$	0
	$\rightarrow c - C_3H$	0
R2(RR) ^a	$H + 1 - C_3H \rightarrow 1 - C_3H_2$	0
	$\rightarrow c - C_3H_2$	0
R3(RR) ^a	$H + c - C_3H \rightarrow c - C_3H_2$	0
	$\rightarrow 1 - C_3H_2$	0
R4(NR) ^a	$H + c, 1 - C_3H_2 \rightarrow C_3H_3(CH_2CCH)$	0
R5(RR) ^a	$H + C_3H_3 \rightarrow CH_3CCH$	0
	$\rightarrow CH_2CCH_2$	0
R6(NR) ^a	$H + CH_3CCH \rightarrow C_3H_5$	2013
R7(NR) ^b	$H + CH_2CCH_2 \rightarrow C_3H_5$	0
R8(RR) ^a	$H + C_3H_5 \rightarrow C_3H_6$	0
R9(NR) ^a	$H + C_3H_6 \rightarrow C_3H_7$	1600
R10(RR) ^a	$H + C_3H_7 \rightarrow C_3H_8$	0
R11(NR) ^a	$H + C_3H_8 \rightarrow C_3H_7 + H_2$	4000
R12(NR)	$O(^3P) + C_3H_6 \rightarrow CH_3COCH_3$	28.6 ^c
R13(NR)	$O(^3P) + C_3H_6 \rightarrow CH_3CH_2CHO$	30.6 ^c
R14(NR)	$O(^3P) + C_3H_6 \rightarrow 1 - \text{methyl vinyl alcohol}$	32.8 ^c
R15(NR)	$O(^3P) + C_3H_6 \rightarrow 2 - \text{methyl vinyl alcohol}$	33.8 ^c
R16(NR)	$O(^3P) + C_3H_6 \rightarrow \text{PrO}$	40 ^d
R17(NR)	$O(^1D)/O^+ + C_3H_6 \rightarrow \text{PrO}$	^e
R18(NR)	$CH + C_2H_6 \rightarrow C_3H_6 + H$	branching ratio 0.25 ^e
R19(NR)	$CH + C_2H_6 \rightarrow C_2H_4 + CH_3$	branching ratio 0.75 ^e

^aHickson et al. (2016), ^b(<http://kinetics.nist.gov/kinetics/>), ^cThis work, ^dWard & Price (2011), ^eBergantini et al. (2018)

Table 2. Kinetics of the reaction between C_3H_6 and O.

Reaction number (type)	Reaction	Enthalpy of the reaction (Kcal/mol)	
		Gas phase	Ice phase
		(scaled E_a in K) (rate @30K in $\text{cm}^3 \text{s}^{-1}$)	(scaled E_a in K) (rate @25K in s^{-1})
R12(NR)	$O(^3P) + C_3H_6 \rightarrow CH_3COCH_3$	-112.87 (-17.4) (9.7×10^{-14})	-116.17 (28.6) (2.0×10^{-12})
R13(NR)	$O(^3P) + C_3H_6 \rightarrow CH_3CH_2CHO$	-105.88 (-16.3) (9.4×10^{-14})	-108.51 (30.6) (1.6×10^{-12})
R14(NR)	$O(^3P) + C_3H_6 \rightarrow 1 - \text{MVA}$	-98.30 (-15.2) (9.0×10^{-14})	-101.25 (32.8) (1.2×10^{-12})
R15(NR)	$O(^3P) + C_3H_6 \rightarrow 2 - \text{MVA}$	-95.64 (-14.7) (8.9×10^{-14})	-98.05 (33.8) (1.1×10^{-12})
R16(NR)	$O(^3P) + C_3H_6 \rightarrow \text{PrO}$	-81.09 (-12.5) (8.3×10^{-14})	-82.92 (40.0) (5.2×10^{-13})

features of PrO and integral absorption coefficients obtained with high-level quantum chemical methods could be handy for its future detection by the high-resolution Stratospheric Observatory for Infrared Astronomy (SOFIA) and the most awaited JWST. The remainder of this paper is as follows: Section 2 describes the reaction pathways considered in our modeling. In Section 3, we discuss chemical modeling. In Section 4, vibrational spectroscopy is presented. Radiative transfer modeling is discussed in Section 5, and finally, in section 6 we draw our conclusions.

2. Reaction pathways

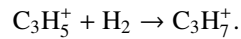
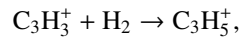
2.1. Methodology

To study the formation and destruction reactions of propylene oxide and associated species, we have considered both gas phase and grain surface reactions. To study the reaction pathways, we have employed quantum chemical methods. We have carried out quantum chemical calculations to find out the reaction enthalpies of these gas/ice phase reactions. In Table 1, we have summarized all the surface reactions which are considered for the formation of propylene and propylene oxide. In Table 2, we have provided the enthalpy of reactions between C_3H_6 and $O(^3P)$ for five (R12-R16)

product channels. Gaussian 09 program (Frisch et al. 2015) has been utilized for such calculations. Here, we have used Density Functional Theorem (DFT) with 6-311G basis set with the inclusion of diffuse (++) along with polarization functions (d,p) and B3LYP functional (Becke 1988; Lee et al. 1988). The Polarizable Continuum Model (PCM) using the integral equation formalism variant (IEFPCM) with the default SCRF method has been used to model the solvation-effect for the computation of enthalpy of the ice phase reactions.

2.2. Formation pathways

Marcelino et al. (2007) had discovered propylene (C_3H_6) towards the TMC-1 by using the IRAM 30m radio telescope. They estimated the column density of propylene $\sim 4 \times 10^{13} \text{ cm}^{-2}$. Herbst et al. (2010) studied the formation of gas phase propylene in the cold interstellar cloud. They proposed that propylene could mainly be formed by the dissociative recombination of its precursor ion, $H_3CCHCH_3^+$ via $C_3H_7^+ + e^- \rightarrow C_3H_6 + H$. For the formation of $C_3H_7^+$, following reactions were included in UMIST 2012 (McElroy et al. 2013) network:



But recent study by Lin et al. (2013) found that above two reactions contain some activation barrier (25.5 and 24.7 kJ/mol respectively). In the low-temperature regime, it is problematic to overcome such a high barrier in the gas phase and thus the formation of gas phase $C_3H_7^+$ is inadequate by these routes which suggest considering some alternative reaction pathways to enable the formation of C_3H_6 rather than by the electron recombination reaction as proposed by Herbst et al. (2010). Recently, Hickson et al. (2016) proposed some pathways for the formation of C_3H_6 in the ice phase. Here also, we have considered their pathways too for the formation of this species. In Table 1, we have listed the formation and destruction pathways of C_3H_6 found in the literature and calculated in this work. Though we have considered the formation of C_3 on the grain surface, around the low temperature, its formation on the grain surface is not adequate due to the higher binding energy (4000K from the KIDA database) of the C atom. C_3 is efficiently forming on the gas phase, and thus the formation of C_3H_6 begins after the accretion of gas phase C_3 on the grain surface. Sequential hydrogenation reactions (R1-R8 of Table 1) in the ice phase then leads to the formation of C_3H_6 . Most of these hydrogenation reactions are barrier-less (only reaction R6 has some barrier), so these pathways are very efficient for the formation of C_3H_6 in ice phase. Recently, Bergantini et al. (2018) used the reaction between CH and C_2H_6 for the formation of propylene with a branching fraction of 0.25 (R18). We also have considered reaction number R18 and R19 (0.75 branching fraction) of Table 1 in our calculations as well. A high abundance of ice phase species may reflect in the gas phase by various efficient desorption mechanisms such as thermal, non-thermal and cosmic-ray induced desorption.

The gas phase reaction between oxygen atom $O(^3P)$ and propylene (C_3H_6) has been well studied by several authors (Stuhl & Niki 1971; Atkinson & Cvetanov 1972; Atkinson & Pitts 1974; Knya et al. 1992). Branching ratios of the reaction between C_3H_6 and O atom were studied by DeBoer & Dodd (2007). They showed that the propylene and oxygen atom could form a stable bi-radical (CH_3CHCH_2O) having an activation barrier of ~ 7.5 kJ/mol. Dissociation of this bi-radical follows various pathways with both singlet and triplet potential energy surfaces. Isomerization of PrO can produce (a) acetone, (b) propanal (c) methyl vinyl alcohol and (d) ally alcohol. However, all these have to overcome very high activation barriers (Dubnikova & Lifshitz 2000) which is not possible at our desired environment.

Ward & Price (2011) described the production of EO and PrO on interstellar dust (graphite surface). They found an activation barrier of about 40 K for the formation of PrO by the reaction between C_3H_6 and $O(^3P)$. Hudson et al. (2017) proposed that the reaction between $O(^3P)$ atom and C_3H_6 can produce any of the following five species, namely, (i) propylene oxide (C_3H_6O), (ii) propanol (CH_3CH_2CHO), (iii) 1-methyl vinyl alcohol (CH_3COHCH_2), (iv) acetone (CH_3COCH_3) and (v) 2-methyl vinyl alcohol ($CH_3CHCHOH$). We have carried out quantum chemical calculations to find out the reaction enthalpies of these gas/ice phase reactions. In Table 2, we have shown the enthalpy of reactions between C_3H_6 and $O(^3P)$ for these five (R12-R16) product channels. Table 2 depicts that in between the five product channels (R12-R16), production of acetone is comparatively most, and production of PrO is least favorable. In Table 1, reaction R12-R16 are arranged according to their exothermicity values obtained from our calculated values in Table 2. Ward & Price (2011) found an activation barrier of about 40 K for the formation of ice phase PrO. We have considered the activation barrier of the other product channels by using a scaling factor based on their exothermicity values obtained from the ice phase reactions of Table 2. The ice phase rate coefficients of these reactions (R12-R16) have been calculated by the method described in Hasegawa, Herbst & Leung (1992), which is based on thermal diffusion. For the binding energy of O, we have used 1660 K (He et al. 2015) and for C_3H_6 , we have used 2580 K (Ward & Price 2011) respectively. For the other species, we have considered the most updated set of energy barriers available in KIDA database. Calculated ice phase rate for these 5 product channels are shown in the last column of Table 2 for ($T_{ice} = 25$ K).

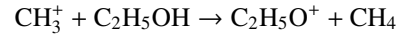
Recently Leonori et al. (2015) computed the rate constant for the formation of gas phase PrO at high temperature for the addition and abstraction reactions interpolated between 300 – 2000 K. According to their results, formation of PrO by the addition of C_3H_6 and $O(^3P)$ can be approximated by the following Arrhenius expression:

$$K = \alpha T^\beta \exp(-E_a/T) \text{ cm}^3 \text{ molecules}^{-1} \text{ s}^{-1},$$

where, $\alpha = 4.52 \times 10^{-16}$, $\beta = 1.406$ and E_a , the activation barrier is -12.5 K. Here, we have assumed that this reaction is also feasible around the low temperature as well. Using the above

relation, at 30 K, we have a rate of $8.3 \times 10^{-14} \text{ cm}^3 \text{ s}^{-1}$ for the formation of gas phase PrO (R16 of Table 2). Since the activation barrier for the other 4 products resulting from the gas phase reaction between C_3H_6 and O (R12-R15 of Table 2) are yet to be known, we have used their gas phase exothermicity values pointed out in Table 2 to scale the activation barrier (E_a). Thus, for these 4 product channels, we have kept α and β same as the gas phase reaction number R16 of Table 2 and have scaled E_a according to their exothermicity values.

Dickens et al. (1997) proposed the following gas-phase formation pathways of EO:



followed by,

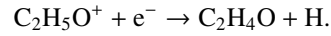


Table 3. Destruction pathways of PrO and its isomers.

Reaction number (type)	Reaction	α	β	γ	Rate coefficient@30 K
R1 (IN)	$C^+ + C_3H_6O \rightarrow C_3H_6O^+ + C$	1.50×10^{-9}	-0.5	0.0	4.74×10^{-09}
R2 (IN)	$C^+ + CH_3CH_2CHO \rightarrow C_3H_6O^+ + C$	1.50×10^{-9}	-0.5	0.0	4.74×10^{-09}
R3 (IN)	$C^+ + CH_3CHCHOH \rightarrow C_3H_6O^+ + C$	1.50×10^{-9}	-0.5	0.0	4.74×10^{-09}
R4 (IN)	$C^+ + CH_3COHCH_2 \rightarrow C_3H_6O^+ + C$	1.50×10^{-9}	-0.5	0.0	4.74×10^{-09}
R5 (IN)	$C^+ + C_3H_6O \rightarrow C_3H_5O^+ + CH$	1.50×10^{-9}	-0.5	0.0	4.74×10^{-09}
R6 (IN)	$C^+ + CH_3CH_2CHO \rightarrow C_3H_5O^+ + CH$	1.50×10^{-9}	-0.5	0.0	4.74×10^{-09}
R7 (IN)	$C^+ + CH_3CHCHOH \rightarrow C_3H_5O^+ + CH$	1.50×10^{-9}	-0.5	0.0	4.74×10^{-09}
R8 (IN)	$C^+ + CH_3COHCH_2 \rightarrow C_3H_5O^+ + CH$	1.50×10^{-9}	-0.5	0.0	4.74×10^{-09}
R9 (IN)	$H^+ + C_3H_6O \rightarrow C_3H_6O^+ + H$	3.60×10^{-9}	-0.5	0.0	1.13×10^{-08}
R10 (IN)	$H^+ + CH_3CH_2CHO \rightarrow C_3H_6O^+ + H$	3.60×10^{-9}	-0.5	0.0	1.13×10^{-08}
R11 (IN)	$H^+ + CH_3CHCHOH \rightarrow C_3H_6O^+ + H$	3.60×10^{-9}	-0.5	0.0	1.13×10^{-08}
R12 (IN)	$H^+ + CH_3COHCH_2 \rightarrow C_3H_6O^+ + H$	3.60×10^{-9}	-0.5	0.0	1.13×10^{-08}
R13 (IN)	$H^+ + C_3H_6O \rightarrow C_3H_5O^+ + H$	3.60×10^{-9}	-0.5	0.0	1.13×10^{-08}
R14 (IN)	$H^+ + CH_3CH_2CHO \rightarrow C_3H_5O^+ + H$	3.60×10^{-9}	-0.5	0.0	1.13×10^{-08}
R15 (IN)	$H^+ + CH_3CHCHOH \rightarrow C_3H_5O^+ + H$	3.60×10^{-9}	-0.5	0.0	1.13×10^{-08}
R16 (IN)	$H^+ + CH_3COHCH_2 \rightarrow C_3H_5O^+ + H$	3.60×10^{-9}	-0.5	0.0	1.13×10^{-08}
R17 (IN)	$He^+ + C_3H_6O \rightarrow HCO + C_2H_5^+ + He$	3.00×10^{-9}	-0.5	0.0	9.48×10^{-09}
R18 (IN)	$He^+ + CH_3CH_2CHO \rightarrow HCO + C_2H_5^+ + He$	3.00×10^{-9}	-0.5	0.0	9.48×10^{-09}
R19 (IN)	$He^+ + CH_3CHCHOH \rightarrow HCO + C_2H_5^+ + He$	3.00×10^{-9}	-0.5	0.0	9.48×10^{-09}
R20 (IN)	$He^+ + CH_3COHCH_2 \rightarrow HCO + C_2H_5^+ + He$	3.00×10^{-9}	-0.5	0.0	9.48×10^{-09}
R21 (IN)	$He^+ + C_3H_6O \rightarrow HCO^+ + C_2H_5 + He$	3.00×10^{-9}	-0.5	0.0	9.48×10^{-09}
R22 (IN)	$He^+ + CH_3CH_2CHO \rightarrow HCO^+ + C_2H_5 + He$	3.00×10^{-9}	-0.5	0.0	9.48×10^{-09}
R23 (IN)	$He^+ + CH_3CHCHOH \rightarrow HCO^+ + C_2H_5 + He$	3.00×10^{-9}	-0.5	0.0	9.48×10^{-09}
R24 (IN)	$He^+ + CH_3COHCH_2 \rightarrow HCO^+ + C_2H_5 + He$	3.00×10^{-9}	-0.5	0.0	9.48×10^{-09}
R25 (IN)	$H_3^+ + C_3H_6O \rightarrow C_3H_7O^+ + H_2$	4.14×10^{-10}	-0.5	0.0	1.29×10^{-09}
R26 (IN)	$H_3^+ + CH_3CH_2CHO \rightarrow C_3H_7O^+ + H_2$	4.14×10^{-10}	-0.5	0.0	1.29×10^{-09}
R27 (IN)	$H_3^+ + CH_3CHCHOH \rightarrow C_3H_7O^+ + H_2$	4.14×10^{-10}	-0.5	0.0	1.29×10^{-09}
R28 (IN)	$H_3^+ + CH_3COHCH_2 \rightarrow C_3H_7O^+ + H_2$	4.14×10^{-10}	-0.5	0.0	1.29×10^{-09}
R29 (IN)	$HCO^+ + C_3H_6O \rightarrow C_3H_7O^+ + CO$	3.40×10^{-9}	-0.5	0.0	1.07×10^{-08}
R30 (IN)	$HCO^+ + CH_3CH_2CHO \rightarrow C_3H_7O^+ + CO$	3.40×10^{-9}	-0.5	0.0	1.07×10^{-08}
R31 (IN)	$HCO^+ + CH_3CHCHOH \rightarrow C_3H_7O^+ + CO$	3.40×10^{-9}	-0.5	0.0	1.07×10^{-08}
R32 (IN)	$HCO^+ + CH_3COHCH_2 \rightarrow C_3H_7O^+ + CO$	3.40×10^{-9}	-0.5	0.0	1.07×10^{-08}
R33 (IN)	$H_3O^+ + C_3H_6O \rightarrow C_3H_7O^+ + H_2O$	3.60×10^{-9}	-0.5	0.0	1.13×10^{-08}
R34 (IN)	$H_3O^+ + CH_3CH_2CHO \rightarrow C_3H_7O^+ + H_2O$	3.60×10^{-9}	-0.5	0.0	1.13×10^{-08}
R35 (IN)	$H_3O^+ + CH_3CHCHOH \rightarrow C_3H_7O^+ + H_2O$	3.60×10^{-9}	-0.5	0.0	1.13×10^{-08}
R36 (IN)	$H_3O^+ + CH_3COHCH_2 \rightarrow C_3H_7O^+ + H_2O$	3.60×10^{-9}	-0.5	0.0	1.13×10^{-08}
R37 (DR)	$C_3H_6O^+ + e^- \rightarrow C_2H_5 + HCO$	1.08×10^{-6}	-0.70	0.0	5.51×10^{-06}
R38 (DR)	$C_3H_6O^+ + e^- \rightarrow CH_3CHCH_2 + O$	1.08×10^{-6}	-0.70	0.0	5.51×10^{-06}
R39 (DR)	$C_3H_6O^+ + e^- \rightarrow CH_2CCH + H_2O + H$	1.50×10^{-7}	-0.50	0.0	4.74×10^{-07}
R40 (DR)	$C_3H_6O^+ + e^- \rightarrow CH_3CCH + H_2O$	1.50×10^{-7}	-0.50	0.0	4.74×10^{-07}
R41 (DR)	$C_3H_7O^+ + e^- \rightarrow C_2H_4 + H_2CO + H$	8.47×10^{-7}	-0.74	0.0	4.67×10^{-06}
R42 (DR)	$C_3H_7O^+ + e^- \rightarrow C_2H_5 + HCO + H$	8.47×10^{-7}	-0.74	0.0	4.67×10^{-06}
R43 (DR)	$C_3H_7O^+ + e^- \rightarrow CO + CH_3CH_3 + H$	8.47×10^{-7}	-0.74	0.0	4.67×10^{-06}
R44 (DR)	$C_3H_7O^+ + e^- \rightarrow H_2CO + C_2H_5$	8.47×10^{-7}	-0.74	0.0	4.67×10^{-06}
R45 (DR)	$C_3H_7O^+ + e^- \rightarrow C_3H_6 + H$	3.00×10^{-7}	-0.74	0.0	1.64×10^{-06}
R46 (DR)	$C_3H_7O^+ + e^- \rightarrow CH_3CH_2CHO + H$	3.00×10^{-7}	-0.74	0.0	1.64×10^{-06}
R47 (DR)	$C_3H_7O^+ + e^- \rightarrow CH_3CHCHOH + H$	3.00×10^{-7}	-0.74	0.0	1.64×10^{-06}
R48 (DR)	$C_3H_7O^+ + e^- \rightarrow CH_3COHCH_2 + H$	3.00×10^{-7}	-0.74	0.0	1.64×10^{-06}
R49 (DR)	$C_3H_5O^+ + e^- \rightarrow CH_3CHO + H$	3.00×10^{-7}	-0.74	0.0	9.48×10^{-07}
R50 (DR)	$C_3H_5O^+ + e^- \rightarrow C_2H_5 + CO$	3.00×10^{-7}	-0.74	0.0	9.48×10^{-07}
R51 (NR)	$CH_3CHCH_2 + O \rightarrow C_2H_5 + HCO$	3.6×10^{-12}	0.0	0.0	3.60×10^{-12}
R52 (NR)	$CH_3CHCH_2 + O \rightarrow CH_3CO + CH_3$	4.4×10^{-12}	0.0	0.0	4.40×10^{-12}
R53 (NR)	$CH_2CHCH_2 + N \rightarrow CH_2CHCN + H_2$	3.2×10^{-11}	0.17	0.0	2.16×10^{-11}
R54 (NR)	$CH_2CHCH_2 + N \rightarrow C_2H_4 + HCN$	3.2×10^{-11}	0.17	0.0	2.16×10^{-11}
R55 (NR)	$CH_2CHCH_2 + N \rightarrow C_3H_4 + NH$	1.3×10^{-11}	0.17	0.0	8.78×10^{-12}
R56 (NR)	$CH_3CHCH + N \rightarrow CH_2CHCN + H_2$	3.2×10^{-11}	0.17	0.0	2.16×10^{-11}
R57 (NR)	$CH_3CHCH + N \rightarrow C_2H_4 + HCN$	3.2×10^{-11}	0.17	0.0	2.16×10^{-11}
R58 (NR)	$CH_3CHCH + N \rightarrow C_3H_4 + NH$	1.3×10^{-11}	0.17	0.0	8.78×10^{-12}
R59 (PH)	$CH_3CHCH_2 + PHOTON \rightarrow C_2H_4 + CH_2$	1.13×10^{-09}	0.00	1.6	1.56×10^{-30}
R60 (CRPH)	$CH_3CHCH_2 + CR - PHOTON \rightarrow C_2H_4 + CH_2$	1.30×10^{-17}	0.00	750	1.95×10^{-14}

Following the same trend as EO, here also, we have assumed that all the isomers of PrO could also be produced by the dissociative recombination of $C_3H_7O^+$ with the same rate. Formation of $C_3H_7O^+$ ($CH_3COCH_4^+$, i.e., protonated acetone or ethyl, 1- methoxy -, ion) was already included in the UMIST 2012 network, so we have not used any additional channel to form this ion. Instead, only the destruction of this ion by the dissociative recombination is considered.

2.3. Formation by supra-thermal oxygen

Recently, Bergantini et al. (2018) carried out a combined theoretical and experimental work to study the formation of interstellar PrO. They found that the galactic cosmic ray induced ice phase chemistry with the supra-thermal oxygen (O^* or $O(^1D)$) may lead to the significant amount of PrO (R17 of Table 1). For the generation of supra-thermal oxygen, they considered the dissociation of CO_2 , H_2O and CO . The rate constants of the radiolysis were calculated by using the following relation:

$$R = \frac{\zeta}{10^{-17}[s^{-1}]} \frac{G}{100[eV]} S_e \phi_{ism} \text{ s}^{-1},$$

where, G is the radiolysis yield per 100eV, S_e is the electronic stopping cross section, Φ_{ism} is the interstellar cosmic ray flux and ζ is the cosmic ray ionization rate. Here, we have used same G value as used in Bergantini et al. (2018) (2.23, 0.7 and 0.8 for CO_2 , H_2O and CO respectively), $\phi_{ism} = 10 \text{ cm}^{-2} \text{ s}^{-1}$ following Abplanalp et al. (2016). We have used $\zeta = 1.3 \times 10^{-17} \text{ s}^{-1}$ instead of 1.3×10^{-16} used in Bergantini et al. (2018). Though Abplanalp et al. (2016) mentioned that S_e is the electron stopping cross section for electrons, Bergantini et al. (2018) used S_e as the electron stopping cross section for protons from the PSTAR programme. Here, we have used ESTAR programme as used by Abplanalp et al. (2016) (<https://physics.nist.gov/PhysRefData/Star/Text/ESTAR.html>) for the computation of the S_e parameter. Since, S_e is sensitive to the projectile energy, for a better approximation for S_e , we have used projectile energy of the electron 1 KeV (minimum available value in the ESTAR programme), 5 keV and 10 KeV respectively and have considered their average. We have found $S_e = 3.62 \times 10^{-15}$, 1.80×10^{-15} and $2.34 \times 10^{-15} \text{ ev cm}^2/\text{molecule}$ when we have used CO_2 , H_2O and CO ice as target materials respectively. For the density of the target materials, we have used 1.3, 1 and 0.81 gm/cm^3 respectively for CO_2 , H_2O and CO ice from Lauck et al. (2015) and references therein. By considering these S_e parameters, we have obtained rate constants of 1.05×10^{-13} , 1.64×10^{-14} and $2.43 \times 10^{-14} \text{ s}^{-1}$ respectively for CO_2 , H_2O and CO ice as a target material.

For the consideration of the supra-thermal oxygen ($O(^1D)$) in our network, we have considered some trivial approximations. After the generation of these supra-thermal oxygens, they are treated similarly as the $O(^3P)$, except the reaction with C_3H_6 . For the reaction between C_3H_6 and $O(^1D)$, we have assumed that the reaction is barrier-less in nature and process in each encounter. The binding energy of the $O(^1D)$ is assumed to be the same as $O(^3P)$ and supposed to behave similarly in the gas phase upon its sublimation. We have not considered the $O(^1D)$ insertion reactions for any other species in our network. We have used it only for the formation of PrO. We have tested

the effect of this oxygen insertion reaction on the abundances of the major species which remain mostly unaltered.

2.4. Destruction pathways

All the destruction pathways for the PrO along with its isomers are shown in Table 3. We have considered Ion-Neutral (IN) reactions for the destruction of PrO and its isomers. The most abundant ions like, C^+ , H^+ , He^+ , H_3^+ , H_3O^+ , and HCO^+ have been considered (Occhiogrosso et al. 2012). Additionally, dissociative recombination (DR), photo-dissociation (PH) and dissociation by cosmic rays (CRPH) have also been considered for the destruction. Ion-Neutral reactions are very efficient for the destruction of neutral interstellar species. If the neutral species is non-polar, we have used the Langevin collision rate coefficient (Herbst 2006; Wakelam et al. 2010) and if the neutral species is polar, then we have employed the trajectory scaling relation (Su & Chesnavich 1982; Woon & Herbst. 2009). For the destruction by photo-reactions, we have used the following equation:

$$k_{PH} = \alpha \exp(-\gamma A_V), \quad (1)$$

where, α is the rate coefficient (s^{-1}) in the unshielded interstellar ultraviolet radiation field, A_V is the visual extinction and γ controls the extinction of the dust at the ultraviolet wavelength. Here, we have used $\alpha = 1.13 \times 10^{-09} s^{-1}$, and $\gamma = 1.6$ for the photo-dissociation of CH_3CHCH_2 .

For the cosmic-ray-induced photo-reactions, we have used the following relation (Gredel et al. 1989):

$$k_{CRPH} = \alpha \gamma' / (1 - \omega), \quad (2)$$

where, α is the cosmic-ray ionization rate (s^{-1}), γ' is the number of photo-dissociative events that take place per cosmic-ray ionization and ω is the dust grain albedo in the far ultraviolet. Here, we have used $\omega = 0.6$, $\alpha = 1.3 \times 10^{-17} s^{-1}$, and $\gamma' = 750.0$ by following the cosmic ray induced photo-reactions of CH_3OH in Woodall et al. (2007).

3. Chemical Modeling

Here, we have used our large gas-grain chemical network (Das et al. 2008b, 2013a,b; Majumdar et al. 2014a,b; Das et al. 2015a,b; Gorai et al. 2017a,b) to estimate the formation of PrO in the star forming region. The gas phase chemical network is mainly adopted from the UMIST 2012 database (McElroy et al. 2013), and grain surface chemical network is primarily developed from Ruaud et al. (2016). As the initial elemental abundances (Table 4), we have considered the “low metal” abundance having C/O ratio ~ 0.607 (Hincelin et al. 2011) which are often used for the modeling of dense clouds where the majority of the hydrogen atoms are locked in the form of hydrogen molecules.

Table 4. Initial elemental abundances with respect to total hydrogen nuclei.

Species	Abundance
H ₂	5.00×10^{-01}
He	0.90×10^{-01}
N	6.20×10^{-05}
O	2.80×10^{-04}
C	1.70×10^{-04}
Na	2.00×10^{-09}
Mg	7.00×10^{-09}
Si	8.00×10^{-09}
P	2.00×10^{-10}
S	8.00×10^{-08}
Cl	1.00×10^{-09}
Fe	3.00×10^{-09}

3.1. Dark cloud model

3.1.1. Physical condition

To mimic the observed region of the PrO, we have considered a total hydrogen number density (n_H) = 2×10^4 cm⁻³ and a gas temperature (T_{gas}) = 30 K and dust temperature (T_{ice}) = 10 and 25 K respectively. A visual extinction parameter (A_V) of 30 have been assumed and a cosmic ray ionization rate (ζ) of 1.3×10^{-17} s⁻¹ (Herbst 1973) been considered. Since the reactive desorption (Garrod, Wakelam & Herbst 2007) is a very efficient means to transfer surface species into the gas phase upon formation, we have considered it in our model.

3.1.2. Results & Discussions

Chemical evolution of PrO and C₃H₆ is shown in Fig. 2. The left panel of Fig. 2 is for $T_{ice} = 10$ K and right panel is for $T_{ice} = 25$ K. Left panel depicts two scenarios, and one is with a fiducial reactive desorption parameter $a = 0.03$, unless otherwise stated, we always have used this value of desorption factor along with the desorption probability 1 (for the reactions producing single product) and another with $a = 0$. It shows that when reactive desorption parameter is absent ($a = 0$), the formation of PrO is insignificant in both the phases. The reason behind is that C₃H₆ can efficiently be formed on ice phase but when $a = 0.03$ is considered, significant portion of C₃H₆ can be able to transfer to the gas phase which is not possible for $a = 0$. Woodall et al. (2007) considered barrier-less reactions for the formation of C₃H₅⁺ and C₃H₇⁺ in gas phase. But it is already discussed in section 2.2 that these two reactions contain high barrier and it is quite problematic to overcome such a high obstacle around low temperature. Moreover, due to high energy barrier of O atom (1660 K for ground state oxygen and supra-thermal oxygen atom), oxygenation reaction is not as fast as hydrogenation reaction in low temperature ($T_{ice} = 10$ K) and thus ice phase PrO formation is inadequate in low temperature. At the low temperature (~ 10 K) PrO can mainly be formed in the gas phase by the reaction between O atom and C₃H₆, where the major contribution of C₃H₆ is coming from the ice. As we have increased the temperature (right panel, $T_{ice} = 25$ K), the situation has changed because of the increase in the mobility of O atom on grain which enables a significant production of PrO on the grain surface. From our Dark cloud model (for $a = 0.03$ and $T_{ice} = 10$ K), in between our simulation time scale ($\sim 10^6$ years), we have a peak abundance (w.r.t. H₂) of

PrO to be 4.17×10^{-14} and 5.26×10^{-14} respectively in gas and ice phase whereas for $a = 0.03$ and $T_{ice} = 25$ K it is 1.33×10^{-11} and 2.04×10^{-7} respectively. In order to check the dependency of our result on the fiducial factor, we further have considered $a = 0.01$ and $T_{ice} = 25$ K and found that the peak gas phase abundance ($\sim 4.58 \times 10^{-12}$) decreased by ~ 3 times compared to the case with $a = 0.03$ and $T_{ice} = 25$ K.

Since, the abundance of C_3H_6 in the gas phase is not adequate, no significant amount of PrO is obtained for $T_{ice} = 10$ K but for $T_{ice} = 25$ K, formation of C_3H_6 significantly enhanced and resulting significant increase in the production of PrO. To find out a parameter space for the formation of PrO in the dark cloud condition, we have varied the number density of total hydrogen (n_H) in between $10^4 - 10^7$ cm^{-3} and ice temperature between 10 – 25 K and kept the gas temperature at 30 K. The resulting plot is shown in Fig. 3. It is clear from the plot that the observed abundance ($\sim \times 10^{-11}$) of PrO can be obtained in between $n_H = 10^4 - 10^5$ cm^{-3} and ice temperature range 20 – 25 K.

Since, we have considered a small activation barrier of about 40 K for the ice phase reaction between C_3H_6 and $O(^3P)$, consideration of supra-thermal oxygen has not influenced our results. It would be kept in mind that due to the unavailability of the binding energy values for $O(^1D)$, we have considered the same binding energy as it was for $O(^3P)$. However, it is expected that due to the generation process of the supra-thermal oxygen, it would carry some extra energy which would enable it to move much faster than $O(^3P)$. Thus, it is expected that the binding energy of $O(^1D)$ would be lower than $O(^3P)$. We have tested the abundance of PrO again by considering a lower binding energy value (half of the normal oxygen) for $O(^1D)$. However, again for this case, we have not found any significant difference. The reason behind is that in one hand lower binding energy provides much faster diffusion rate and enhances the chance of recombination, but on another hand, it gives much quicker sublimation rate which decreases the residence time of $O(^1D)$ on the grain surface and thus reduces the chance of recombination. Since in our network, PrO mainly formed by the reaction between C_3H_6 and $O(^3P)$, lowering the binding energy of $O(^1D)$ have not changed our PrO abundance. A higher dose of cosmic rays would be useful to generate more supra-thermal oxygen which could be helpful in the PrO formation, but it would also dissociate PrO as well. We think that the cosmic ray ionization rate of about 1.3×10^{-17} s^{-1} which is used here, is a standard value for the region where the three transitions of PrO had been observed.

3.2. Hot core model

3.2.1. Physical condition

Cunningham et al. (2007) attempted to observe PrO and glycine in Sgr B2(LMH) and Orion-KL by using MOPRA telescope. However, they did not detect either species but were able to put an upper limit on the abundances of these two molecules in these sources. They proposed an upper limit of about 6.7×10^{14} cm^{-2} for the column density of PrO in Sgr B2 (LMH). Here, to estimate

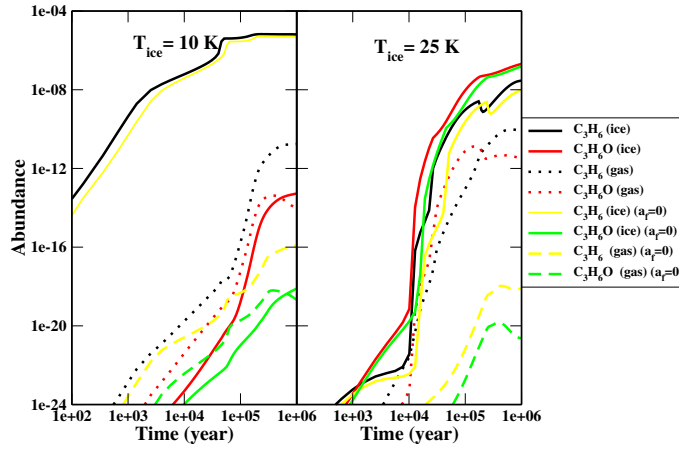


Fig. 2. Chemical evolution of PrO and C₃H₆ for a dark cloud model. Solid line represents ice phase abundance and dotted line represents the gas phase abundance.

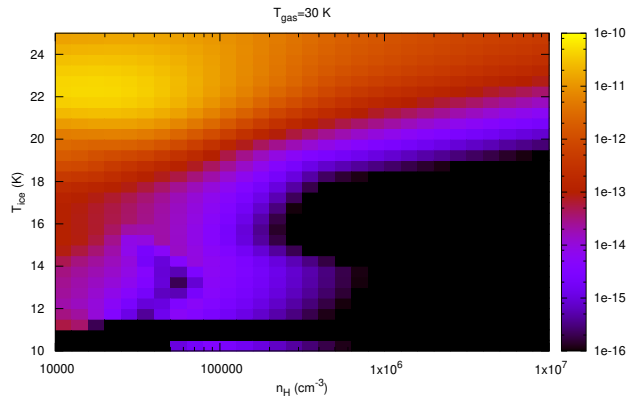


Fig. 3. Parameter space of the abundance of PrO in dark cloud conditions. Color bar represents the fraction abundance of PrO

Table 5. Vibrational analysis of propylene oxide using B3LYP/6-311++G(d,p)

Wavenumber	Integral	Ab-	Band assignment	Exp.
$\nu(\text{cm}^{-1})$	sorbance	sorbance		value
$\lambda(\mu\text{m})$	Coefficient(cm molecule^{-1})	sorbance		(Hudson et al. 2017)
218.85	45.84	1.31×10^{-19}	CH ₃ torsion	
367.62	27.20	1.23×10^{-18}	CCC bending	
411.41	24.30	1.19×10^{-18}	CCO bending	
752.24	13.29	$2.47 (1.43)^a \times 10^{-18}$	ring deformation	742.0
826.19	12.10	$15.6 (9.53)^a \times 10^{-18}$	ring deformation	825.9
905.22	11.04	$8.69 (4.8)^a \times 10^{-19}$	CH ₂ rocking	896.7
961.52	10.40	$4.23 (2.35)^a \times 10^{-18}$	CC stretching or CH ₃ rocking	948.3
1038.38	9.63	$3.08 (2.46)^a \times 10^{-18}$	CH ₃ wagging	1027.3
1119.31	8.93	2.01×10^{-18}	CH ₂ rocking	
1149.97	8.69	8.84×10^{-19}	CH ₂ wagging	
1163.75	8.59	8.85×10^{-19}	CH ₃ bending	
1185.69	8.43	2.54×10^{-19}	CH bending	
1291.89	7.74	$1.52 (1.47)^a \times 10^{-18}$	CH bending, ring deformation	1266
1401.63	7.13	$7.90 (2.57)^a \times 10^{-19}$	CH ₃ deformation	1408
1434.36	6.97	5.23×10^{-18}	CC stretching	
1473.10	6.78	1.70×10^{-18}	CH ₃ deformation	
1486.40	6.72	1.78×10^{-18}	CH ₃ deformation	
1520.59	6.57	1.98×10^{-18}	CH ₂ scissoring	
3027.69	3.30	3.98×10^{-18}	CH ₃ symmetric stretching	
3087.79	3.24	5.92×10^{-18}	CH ₂ asymmetric stretching	
3089.63	3.23	4.84×10^{-18}	CH ₂ symmetric stretching	
3098.32	3.22	1.12×10^{-18}	CH stretching	
3116.85	3.20	1.02×10^{-17}	CH stretching	
3179.24	3.14	5.70×10^{-18}	CH ₂ asymmetric stretching	

^a Hudson et al. (2017).

Table 6. Vibrational analysis of protonated propylene oxide ($C_3H_6OH^+$) using B3LYP/6-311++G(d,p)

Wavenumber $\nu(\text{cm}^{-1})$	Integral Absorbance $\lambda(\mu\text{m})$ Coefficient(cm molecule^{-1})	Band assignment
207.33	48.23	8.78×10^{-20} CH ₃ torsion
325.32	30.73	4.77×10^{-18} CCO bending
395.82	25.26	2.25×10^{-18} CCC bending
494.41	20.22	9.16×10^{-18} ring deformation
748.95	13.35	2.56×10^{-17} CO stretching
845.94	11.82	1.06×10^{-17} OH torsion
894.73	11.17	1.03×10^{-17} CC stretching
936.21	10.68	1.48×10^{-18} CH ₃ wagging, CH ₂ torsion
982.36	10.17	5.08×10^{-18} CH ₂ rocking, OH bending
1034.35	9.66	6.07×10^{-18} CH ₃ wagging
1134.12	8.81	1.72×10^{-18} CH, CH ₃ bending
1212.99	8.24	5.40×10^{-19} CH ₂ wagging
1225.73	8.15	6.52×10^{-18} CH, OH bending
1231.93	8.11	1.33×10^{-18} CH ₃ bending
1303.36	7.62	2.82×10^{-18} CC stretching
1404.63	7.11	1.43×10^{-18} CH ₃ deformation
1432.85	6.97	4.37×10^{-18} CH ₃ deformation
1463.20	6.83	3.78×10^{-18} CH ₃ deformation
1492.42	3.30	6.70×10^{-18} CH ₃ deformation
1512.84	3.24	6.61×10^{-18} CH ₂ scissoring
3045.28	3.28	6.32×10^{-20} CH ₃ symmetric stretching
3113.53	3.21	5.32×10^{-19} CH ₃ asymmetric stretching
3146.53	3.17	7.45×10^{-19} CH ₂ asymmetric stretching
3165.61	3.15	5.55×10^{-20} CH ₂ symmetric stretching
3201.52	3.12	1.5×10^{-19} CH stretching
3274.58	3.05	5.14×10^{-19} CH ₂ asymmetric stretching
3675.89	2.74	5.45×10^{-17} OH stretching

the abundance of PrO in the hot core region, we have considered a two-phase model as used by Garrod & Herbst (2006). The first phase is assumed to be isothermal at 10 K or 25 K and lasts for 10^6 years. For this phase, we have considered $A_V = 30$ and $\zeta = 1.3 \times 10^{-17} \text{ s}^{-1}$. The subsequent phase is assumed to be a warm-up period where the temperature can gradually increase up to 200 K in 10^5 years. So our total simulation time is restricted up to a total 1.1×10^6 years. The number density of the total hydrogen is assumed to be constant ($n_H = 10^4 - 10^7 \text{ cm}^{-3}$) in both the phases of our simulation.

3.2.2. Results & Discussions

In Fig. 4, we have shown the chemical evolution of PrO for various density clouds ($n_H = 10^4 - 10^7 \text{ cm}^{-3}$). The last panel shows the abundance variation of peak gas phase abundance and final abundance (i.e., at the end of the simulation the time scale $\sim 1.1 \times 10^6$ year) of PrO with the number density variation. In case of the $T_{ice} = 10$ K, as we have decreased the density, gas phase abundance of PrO increased slightly and have a maximum ($\sim 1.5 \times 10^{-7}$ w.r.t. H_2) around $n_H = 1 \times 10^4 \text{ cm}^{-3}$. In the high density region ($\sim 10^7 \text{ cm}^{-3}$), we have obtained the peak abundance $\sim 1.3 \times 10^{-9}$. The final abundance for this case, varies in between $1.4 \times 10^{-10} - 8.9 \times 10^{-8}$. In case of $T_{ice} = 25$ K, the peak and final abundance roughly remain invariant (peak abundance varies in between $1.03 \times 10^{-7} - 2.4 \times 10^{-7}$ and final abundance varies in between $1.7 \times 10^{-8} - 3.5 \times 10^{-8}$).

3.3. Comparison with the previous modeling results

There are some basic differences between the model described above and used by the other authors to explain the observed abundance of PrO. Recently, Bergantini et al. (2018) used a combined experimental and theoretical study to explain the abundance of PrO in the ISM. They explained the

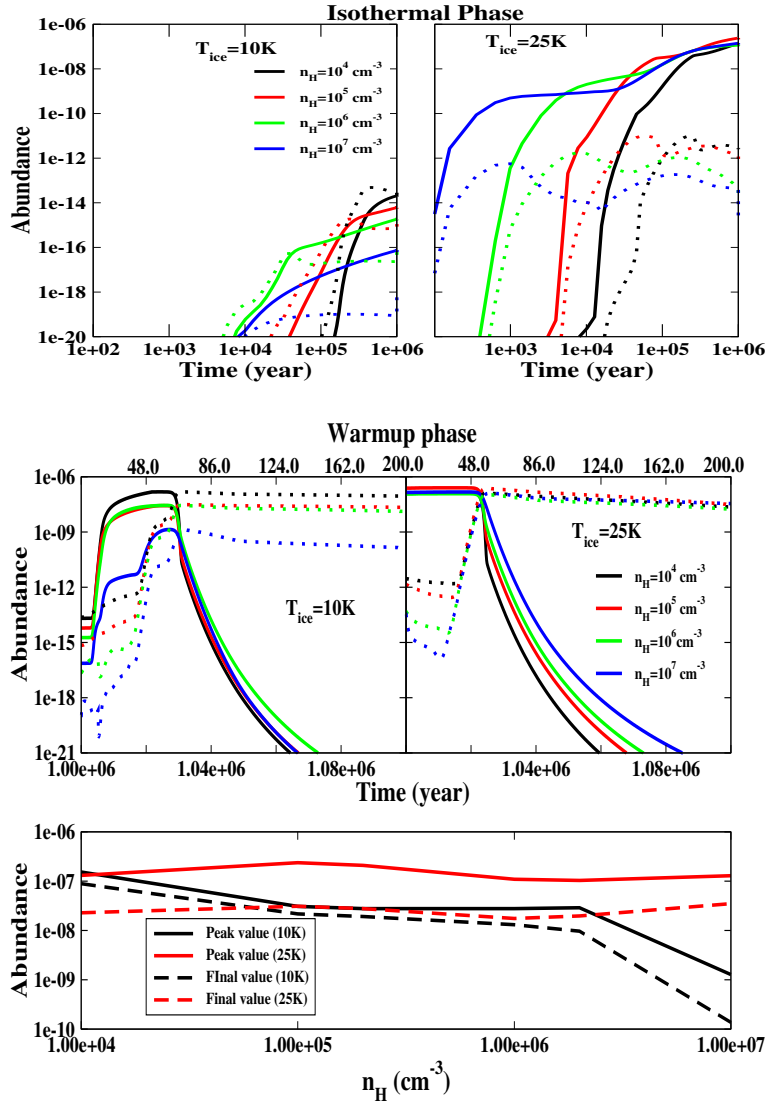


Fig. 4. Chemical evolution of PrO in a Two phase model by considering various density cloud. The upper two panels are for the isothermal phase, middle two panels are for the warm-up, and the lower panel is for the gas phase peak abundance of PrO and final abundance of PrO at the warm-up phase for various density cloud. Different colors are used to denote different density cloud. In the upper and middle panels, the solid line represents the abundance in the gas phase whereas the dotted line represents the abundance in ice phase.

formation of PrO by non-equilibrium reactions initiated by the effects of secondary electrons. More specifically, they used supra-thermal (^1D) oxygen insertion reaction with propylene to explain the PrO formation. They did not consider the formation of PrO by the addition of ground state oxygen (^3P). In our case, we have considered the formation of PrO by both types of oxygen atoms. Ward & Price (2011) found a low activation barrier ($\sim 40\text{K}$) for the ice phase reaction between C_3H_6 and $\text{O}(^3\text{P})$. Such a low activation barrier could be overcome at the low temperature. As a result, we have found an adequate production of PrO even in the absence of the supra-thermal oxygen insertion reaction.

4. Vibrational Spectroscopy

4.1. Methodology

To compute the vibrational transitions of PrO and its protonated form, we have used Gaussian 09 program. We have used the Density Functional Theorem (DFT) with 6-311G basis set including diffuse and polarization functions for this calculations. Initially, we have verified our results with various methods and basis sets and compared it with the experimentally obtained results. We have found that B3LYP/6-311++G(d, p) method is best suited to reproduce the experimentally obtained transitions of PrO. Moreover, we also have considered IEPCM model with the method mentioned above to compute the vibrational transitions of PrO in the ice phase. All optimized geometry was verified by harmonic frequency analysis (having no negative frequency). We have performed our calculations by placing the solute (species) in the cavity within the solvent (water molecule) reaction field. Here, we have used the SCRF method by following the earlier study of Woon (2002).

4.2. Results and discussions

In Table 5, we have summarized calculated and experimental vibrational frequencies of PrO along with the integral absorption coefficients and band assignments. Similarly, Table 6 presents the determined vibrational frequencies along with the integral absorption coefficient of protonated PrO. Our calculated values of absorption coefficients and vibrational frequencies are in excellent agreement with the experimentally obtained results (Hudson et al. 2017). Puzzarini et al. (2014) studied the spectroscopic details of protonated oxirane ($C_2H_5O^+$). Similarly, protonation of PrO can take place. PrO could be protonated via ion-neutral reactions where the proton is transferred to the neutral. Protonated PrO may be formed in the gas phase by the reaction of PrO with the ions like H_3O^+ , HCO^+ and H_3^+ . We have found a proton affinity of PrO about 803.169 kJ/mol by doing quantum chemical calculations (using the HF/6-31G(d) method) which is in an excellent agreement with Hunter & Lias (1998) (803.3 kJ/mol). For another protonated form of PrO, proton affinity value is found to be 801.827 kJ/mol. Thus, protonated PrO shown in Fig. 1c possessing a slightly higher energy (about 175 K) than protonated PrO shown in Fig. 1b. Since the experimental data for protonated PrO is yet to be published, based on the accuracy obtained for the vibrational transitions of PrO, same method and basis set have been applied for protonated PrO to compute the vibrational transitions and integral absorption coefficients. Figure 5ab depicts the absorption spectra of PrO and its protonated form. Figure 5a covers 1600 – 200 cm^{-1} region (some parts of the mid IR: 2000 – 400 cm^{-1} and some parts of the far IR: 400 – 50 cm^{-1}) and Fig. 5b covers 3800 – 3000 cm^{-1} region (i.e., some parts of the near IR: 12800 – 2000 cm^{-1}).

4.3. Comparison with the experimentally obtained results

In the top and bottom panel of Fig. 6a comparison between our computed and experimentally obtained vibrational spectra is shown for (1600 – 800) cm^{-1} and (3200 – 2700) cm^{-1} frequency

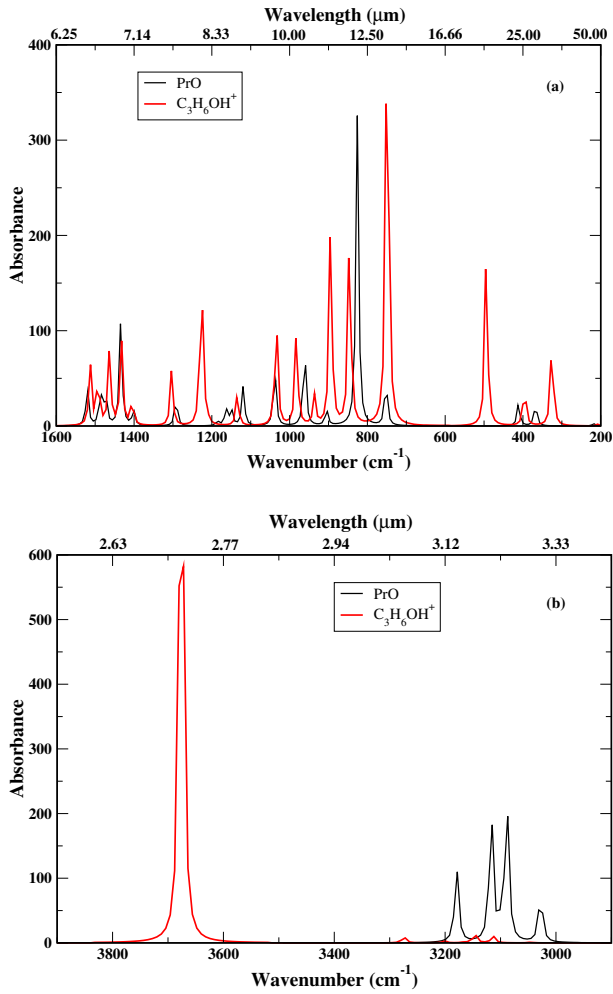


Fig. 5. Comparison between our calculated IR spectra of Propylene Oxide and protonated propylene oxide.

window respectively. In these two panels, we also have shown how the clustering of PrO can affect the computed vibrational spectra of PrO. The blue line in Fig. 6 represents the experimental data extracted from Hudson et al. (2017) whereas the black, red, and green line represent the calculated spectra with PrO monomer, PrO dimer, and PrO tetramer respectively. Fig. 6a depicts that in the mid-IR region, we have a good agreement between our theoretical and experimental results of Hudson et al. (2017). We have noticed that most of the transitions within this mid-IR region are within an error bar of about 10 cm^{-1} . One transition at 1291.89 cm^{-1} is found to be shifted maximum by 25 cm^{-1} . The intensity of each mode of vibration and the area under the curve of various regime changes with the cluster size of PrO. We have noticed that if a scaling factor of 0.9728 is used, we have an excellent agreement around the stretching mode and thus in Fig. 6b, we have scaled our computed wavenumber accordingly.

5. Radiative transfer modeling

5.1. Methodology

In Astrochemistry, a major aim of radiative transfer modeling is to extract the molecular abundances from the line spectra at infrared and sub(millimeter) wavelengths. Three different levels of radiative

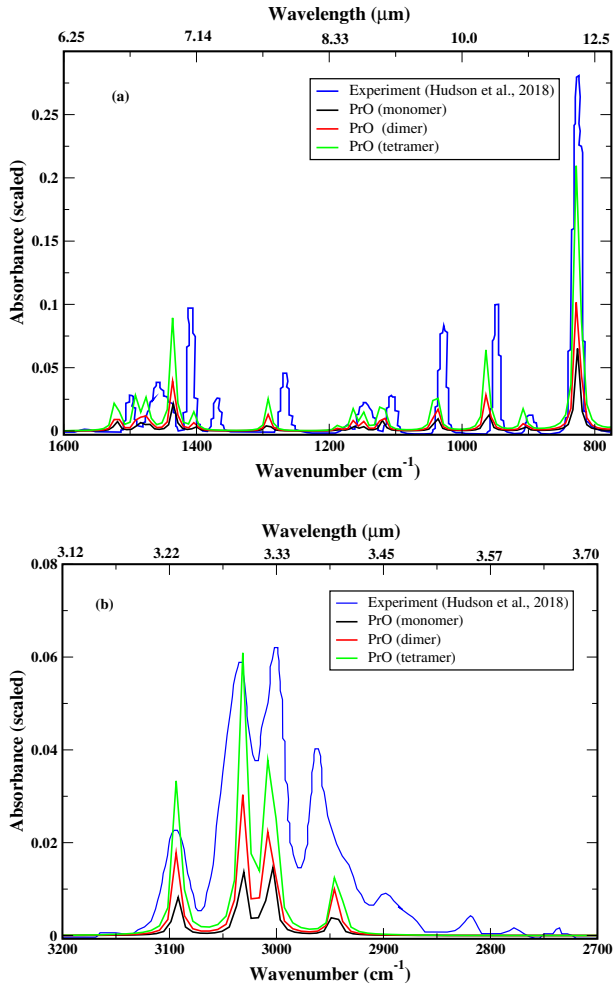


Fig. 6. Comparison between our calculated spectra with that obtained in the experiment (Hudson et al. 2017). Results of (Hudson et al. 2017) has been digitally extracted by using <https://apps.automeris.io/wpd>. In the upper panel, we have shown the mid-IR region and in the bottom panel, we have shown the near-IR region. For the sake of better visualization, we have scaled down the Y axis of our calculated values in (a) and (b). Our calculated wavenumber in X-axis of (b) is scaled by 0.9728 to have better agreement.

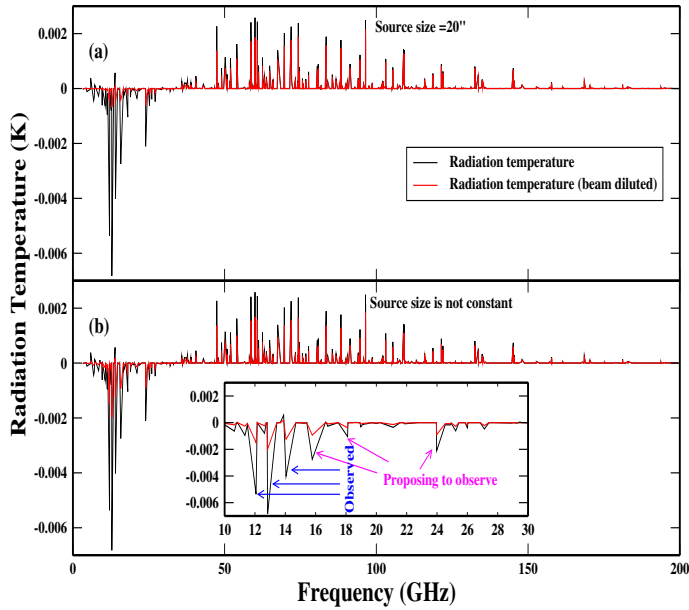


Fig. 7. Line parameters of PrO for non-LTE condition by considering (a) constant source size (20'') and (b) varied source size (Hollis et al. 2007). Observed and other possible transitions are highlighted inside a separate box in Fig. 7.

transfer model are in use which ranges from the basic Local Thermodynamic Equilibrium (LTE) models to complex non-local models in 2D and even more complex models in 3D (Van der Tak 2011).

A simple single excitation temperature model, i.e., LTE modeling has been carried out to predict the most probable transition of PrO. LTE modeling is considered to be a good starting point for predicting the line parameters around the high-density region. Moreover, it does not require additional collisional information. We have used CASSIS program which was developed by IRAP-UPS/CNRS (<http://cassis.irap.omp.eu>) for the LTE modeling. Recently, McGuire et al. (2016) observed 3 transitions of PrO in absorption. Cunningham et al. (2007) used the MOPRA telescope at the 3 mm band for the identification of various transitions of PrO in Sgr B2(LMH) and Orion-KL. However, they were unable to detect any PrO transitions in these two targeted regions but they had provided an upper limit for the abundance of PrO around these sources. We have carried out the LTE calculations for two different cases. First one is for the sources where we are expecting the transitions of PrO in the extended molecular shell around the embedded, massive protostellar object as observed by McGuire et al. (2016) and for the second one, we have considered the input parameters in such a way that we may observe some strong transitions of PrO in the hot core regions as attempted by Cunningham et al. (2007).

In the LTE model, level populations are controlled by Boltzmann distribution. As Interstellar chemical process far from thermodynamic equilibrium, it is essential to consider the non-LTE method where the balance between the excitation and de-excitation of molecular energy levels are explicitly solved. Collisional and radiative both the processes contribute to this balance. Most importantly, for the non-LTE method, the collisional data file is required which is not available for most of the species. Collisional data file for PrO was not available in any database. To have an educated estimation of the line parameters in non-LTE, we have considered the collisional rate parameters of $e - \text{CH}_3\text{OH}$ with H_2 (Rabli & Flower 2010) for preparing the collisional data file of PrO. Since PrO is a slightly asymmetric rotor molecule, it would have been better if we have used the collisional parameters of H_2CO here. But due to the unavailability of the collisional rates for the sufficient number of energy levels for H_2CO , tempted us to use $e - \text{CH}_3\text{OH}$ as an approximation for which we have the collisional parameters available in LAMDA database (Schöier et al. 2005) for sufficient number of energy levels. RADEX program (Van der Tak et al. 2007) have been used for this non-LTE computation.

5.2. Results and discussions

5.2.1. LTE model

For the first case, we have considered the GBT 100m telescopic parameter for the modeling and adopted parameters are shown in Table 7. For this case, we have assumed that the source size (θ_s) 20'' and beam size (θ_b) may vary depending upon the frequency by $\frac{744}{\nu}$ (Hollis et al. 2007), where

Table 7. Input parameters used for the LTE modeling

Parameters used for GBT (100 m) ^a	
Column density of H ₂	10 ²⁴ cm ⁻²
Column density of propylene oxide	1.0 × 10 ¹³ cm ⁻²
Excitation temperature (T_{ex})	5 K
Background temperature (T_C)	2.73 K (default for LTE)
FWHM	15 km/s
Source size (θ_s)	20''
Beam size (θ_b)	$\frac{744}{\nu}$
Beam dilution	$B = \frac{\theta_s^2}{(\theta_s^2 + \theta_b^2)}$
Parameters used for ALMA (400 m) ^b	
Column density of H ₂	10 ²⁴ cm ⁻²
Column density of propylene oxide	1.74 × 10 ¹⁶ cm ⁻²
Excitation temperature (T_{ex})	150 K
Background temperature (T_C)	2.73 K (default for LTE)
FWHM	5 km/s
Source size	3.0''
Beam Dilution	1

^a GBT model parameters are based on McGuire et al. (2016).

^b ALMA parameters are based on the model of this work.

Table 8. LTE line parameters of the various transitions of PrO using GBT.

Frequency (GHz)	$J_{Ka'kc'} - J_{Ka''kc''}$	Intensity (mK)
12.07243 ^a	1 ₁₀ – 1 ₀₁	9.47 × 10 ⁻⁶
12.83734 ^a	2 ₁₁ – 2 ₀₂	1.83 × 10 ⁻⁵
14.04776 ^a	3 ₁₂ – 3 ₀₃	2.82 × 10 ⁻⁵

^aMcGuire et al. (2016)

ν is the frequency in GHz. Beam dilution factor is computed by $B = \frac{\theta_s^2}{(\theta_s^2 + \theta_b^2)}$ and applied on the obtained intensity. The recent observation by McGuire et al. (2016) observed three transitions of PrO in cold molecular shell in front of the bright continuum sources/hot cores within Sgr B2. In Table 8, we have pointed out the obtained LTE parameters for these three transitions only. We have noticed that the obtained intensities are very weak and are even below the RMS noise level of 1 mK. The reason behind this result is that in the CASSIS module of LTE, we have used a constant background continuum temperature of 2.73 K. However, a variable background continuum temperature was required to observe these transitions in absorption. We will get back to the discussion about the absorption feature of these three transitions in the later section of this paper again.

For the second case, we have modeled the LTE transitions of PrO for the hot core region. Here, we have used our computed gas phase PrO abundance $\sim 1.74 \times 10^{-8}$ (final abundance with $n_H = 10^6 \text{ cm}^{-3}$ or $n_{H_2} = 5 \times 10^5 \text{ cm}^{-3}$ with initial dust temperature 25 K). We have used ALMA 400 m telescopic parameter for the modeling of this feature. Here, we have considered source size (1.5''), beam size varies as $\frac{186}{\nu}$ (for ALMA 400m) and the beam dilution effect applied following the same formula ($B = \frac{\theta_s^2}{(\theta_s^2 + \theta_b^2)}$) mentioned above. To verify the potential observability of these PrO transitions, we have checked the blending of these transitions with any other interstellar molecular transitions. Interestingly, we have identified a few intense transitions of PrO in Band 3 (84 – 116 GHz) and Band 4 (125 – 163 GHz) which are not blended. In Table 9, we have pointed out all the potentially observable transitions of PrO in the hot core region. Based on our simple LTE model, we have isolated some strong transitions of PrO. We further have used ALMA simulator to check the integration time required to observe these transitions by ALMA. We have found that for ALMA Band 4 (for e.g 130 GHz), with 20 mK RMS noise, 0.4 km/s spectral resolution and 43 antennas along with the dual polarization, 1 hr on-source integration time is required for 5σ detection of PrO

in Sgr B2 (N) with an angular resolution of $1.5''$. For the similar configuration, 3 hrs on-source integration time is required for Band 3 (e.g 100 GHz) observation with ALMA.

5.2.2. non-LTE

In Fig. 7ab, we have shown our computed radiation temperature for the various transitions of PrO within a wide range of frequency (1 – 200 GHz). Here, our target was to find out the line parameters which are relevant for the observations performed by McGuire et al. (2016). Thus, we have considered, $T_{ex} = 5$ K, column density of PrO $= 1 \times 10^{13} \text{ cm}^{-2}$, FWHM $= 15$ Km/s (for the observed three transitions, McGuire et al. (2016) obtained a FWHM of 11.6, 15.8 and 19.6 respectively and here, we have considered the average of these three FWHMs) and $n_{H_2} = 10^5 \text{ cm}^{-3}$. For this non-LTE model, we have used GBT 100m telescopic parameters. Background continuum temperature measurement was already carried out by Hollis et al. (2007). They showed the observed continuum antenna temperatures by the GBT spectrometer toward SgrB2 (N-LMH). Here, we have considered this variation of background temperature by digitally extracting Fig. 1 of Hollis et al. (2007) by using <https://apps.automeris.io/wpd>. According to the Fig. 1 of Hollis et al. (2007) the changes in continuum temperature beyond 40GHz is very small. Extracting the values from Hollis et al. (2007), we have the continuum temperature ~ 3.35 K at 49GHz. Beyond this, they did not provide any data for the continuum temperature, so we have considered a fixed continuum temperature of about 2.73K beyond 100GHz. In between the 49GHz to 100GHz we have interpolated the continuum temperature from 3.35 – 2.73K. We have considered the variation of beam size, by considering the relation $\sim \frac{744}{\nu}$ (Hollis et al. 2007). In Fig. 7a, we have considered that source size is constant at $20''$ and in Fig. 7b, we have considered the source size variation by using $\theta_s = \frac{143}{\nu^{0.52}}$ (Hollis et al. 2007). Radiation temperatures of the various transitions of PrO have been presented in Fig. 7ab by considering the beam dilution effect and avoiding this effect. Most interestingly, with the given conditions, we have obtained all the three transitions (12.07, 12.8 and 14.04 GHz) in absorptions. Additionally, we have identified three more transitions at 15.78 GHz, 18.1 GHz and 23.98 GHz which might potentially be observed around the same region, where the other three transitions were observed.

We have further worked on these 6 transitions to find out the region where it is showing the absorption feature. In this effort, we have used a wide range of parameter space (by varying the number density and kinetic temperature of the medium) to find out the probable absorption zone for these transitions. We have used the RADEX program again for this purpose. In Fig. 8, we have shown the variation of the radiation temperature depending on the H_2 density ($10^4 - 10^7 \text{ cm}^{-3}$) and kinetic temperature (5 – 35 K). It depicts that the absorptions are prominent around the low kinetic temperature (5 – 10 K) and for $n_{H_2} > 10^4 \text{ cm}^{-3}$. Value of the color box at the end of the panels represents the obtained radiation temperature of the transitions in K.

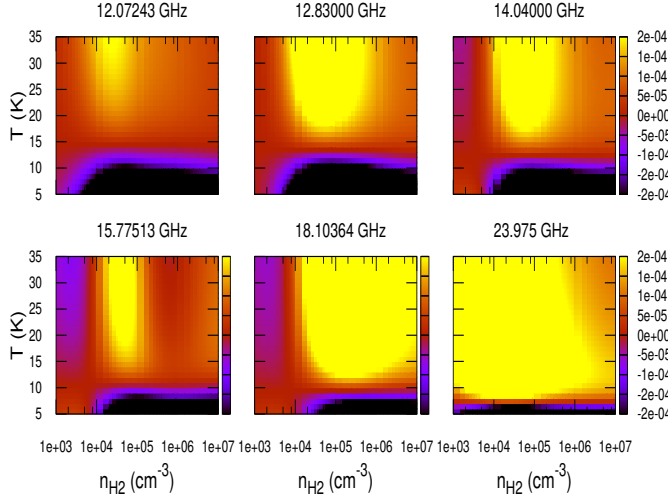


Fig. 8. Parameter space for the radiation temperature of the most probable 6 transitions with non-LTE condition.

In addition to the 3 transition of PrO discussed above, McGuire et al. (2016) observed 18 transitions of acetone and 11 transitions of propanal from PRIMOS survey. To test the fate of these transitions with the collisional rate file adopted from e-CH₃OH, we have calculated the radiation temperature of these transitions for a wide range of parameter space. We have further explored the validity of our collisional data file by checking the computed radiation temperature of propanal and acetone in PRIMOS. In Fig. A1 and Fig. A2 (see Appendix), we have shown the radiation temperature of 11 transitions of propanal and 18 transitions of acetone which were observed in PRIMOS. Fig. A1 shows that for the first six transitions of propanal, we have obtained the absorption feature at $T_{ex} = 5 - 7$ K and relatively at higher densities ($n_{H_2} > 10^5$ cm⁻³). For the transitions at 29.619 GHz and 31.002 GHz, we have obtained the absorption features at relatively lower H₂ density ($10^3 - 10^4$ cm⁻³) and kinetic temperature (10 – 35 K). We have noticed that the last three transitions of propanal are showing emission for the whole range of density and temperature adopted here. Similarly in case of Fig. A2, for the first 14 transitions of acetone, we have obtained the absorption feature within a minimal zone of parameter space, but for the last 4 transitions we have not received the absorption feature. Since then we have seen a significant discrepancy between our calculated and observed radiation temperature at the higher frequencies, it could be attributed due to the unavailability of the collisional rates and its present approximation.

Our non-LTE model accurately reproduces the three observed transitions of PrO in absorption, and for this, we have used observed parameters such as excitation temperature, FWHM, and column density of PrO following McGuire et al. (2016). We have also found a good agreement between the observed transitions of propanal and acetone with our calculated non-LTE transitions. Parameter space for the radiation temperature of the most probable transitions of PrO, propanal, and acetone are presented (Fig. 8, Fig. A1 & Fig. A2) with the non-LTE condition. The similar results obtained by observation (McGuire et al. 2016) and radiative transfer model are used to constrain the physical

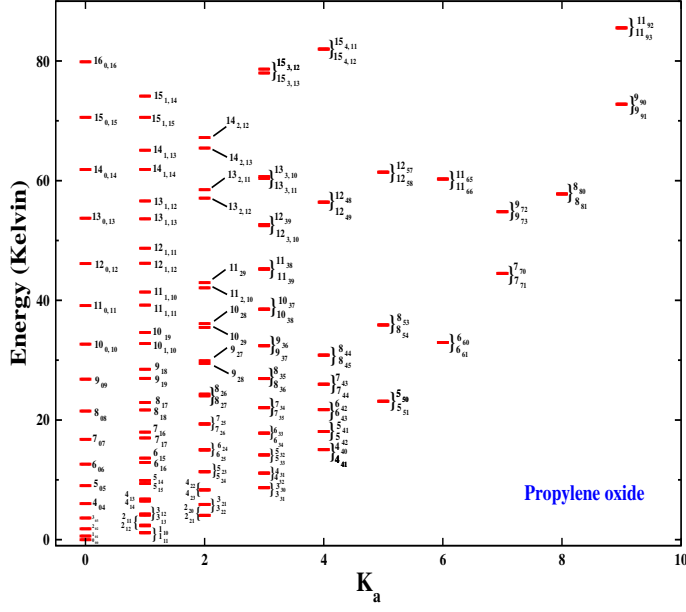


Fig. 9. Rotational energy level diagram of propylene oxide.

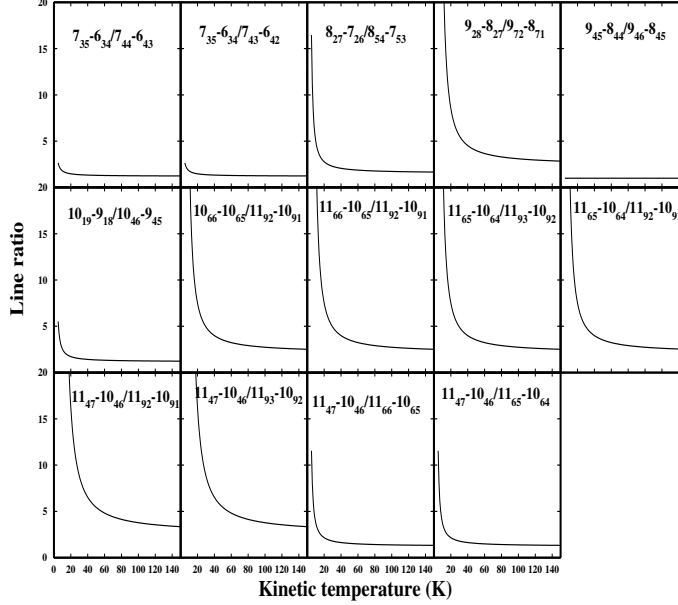


Fig. 10. Variation of line ratio with the kinetic temperature in LTE approximation.

conditions (density, temperature) of that region where these molecules were observed.

In Table 9, we already have pointed out the line parameters of various PrO transitions for the hot core region which lies in ALMA Band 3 and Band 4 regions. For all the transitions shown in Table 9, we have shown the variation of radiation temperature in Fig. A3 for a wide range of parameter space. In constructing the parameter space for the hot core region, we have used $T_{ex} = 5 - 160$ K and $n_{H_2} = 10^4 - 10^7$ cm $^{-3}$. Outside each panel, a color box is placed to show the radiation temperature in K. Fig. A3 would be very useful to know the emission feature of these viable transitions before its real observation.

5.3. Estimation of the physical properties from the obtained line parameters:

Mangum & Wootten (1993) used formaldehyde (H_2CO) molecule to trace kinetic temperature and spatial density within molecular clouds. Normally, symmetric rotor molecules (NH_3 , CH_3CN , $\text{CH}_3\text{C}_2\text{H}$ etc.) are used for the measurements of kinetic temperature. However, due to the spatially variable abundances as well as complex excitation properties, usage of these species are doubtful. The main reason behind the choice of formaldehyde was that it permeates the ISM at a relatively high abundance. Formaldehyde is a slightly asymmetric rotor molecule which should possess closer kinetic temperature sensitivities like purely symmetric rotors. Since PrO is an asymmetric top molecule, the ratio of lines from different J-states would be used as the density tracers and the ratio of lines from the same J-state but different K-states could be used as the probes of the regional temperature.

5.3.1. Kinetic temperature measurements:

In the case of symmetric rotors, $\Delta K_a = 0$ dictates the dipole selection rules. Transitions between other K_a -values are only possible by the collisional excitation. Due to this unique feature, a comparison between the energy level populations from different K_a levels within the same symmetry species may be used as a measure of the kinetic temperature. If we consider the ratio between two transitions which could be measured within the same frequency band, various observational uncertainties could be nullified.

Propylene oxide is an asymmetric rotor. We can check the line ratio of propylene oxide for the measurement of temperature and check the consistency of this method with that obtained for H_2CO . Figure 9 depicts the rotational energy level diagram of propylene oxide. Because of its complexity, PrO is not as widespread as H_2CO . On the other hand, PrO is also a slightly asymmetric top molecule, and thus we can compare the line ratios obtained by the PrO observation with the H_2CO observation to derive the precise kinetic temperature of the source. The collisions primarily connect different K_a ladders of PrO. Thus the relative population occupying the ground states of these two K_a ladders are related by the Boltzmann equation at Kinetic temperature. Based on the selection process of Mangum & Wootten (1993) for the measurement of the kinetic temperature, we have used the following selection rule to have the line ratio between two transitions. Suppose the line ratio (R) between the two transitions is:

$$R = \frac{J_1 K_{a1} K_{c1} - J_2 K_{a2} K_{c2}}{J_3 K_{a3} K_{c3} - J_4 K_{a4} K_{c4}},$$

where, J_i , K_{ai} , K_{ci} ($i = 1, 4$) are used to denote the quantum numbers of the energy levels involved in the transition. We have utilized the following selection rules for the measurement of the kinetic temperature from the line ratio. (a) $\Delta J = 1$ (i.e., $J_1 - J_2 = J_3 - J_4 = 1$), (b) $J_1 = J_3$ and $J_2 = J_4$, (c) $\Delta K_a = 0$ (i.e., $K_{a1} - K_{a2} = K_{a3} - K_{a4} = 0$), (d) $K_{a1} \neq K_{a3}$, $K_{a1} \neq K_{a4}$, $K_{a2} \neq K_{a3}$, $K_{a2} \neq K_{a4}$, (e)

$\Delta K_c = 1$ (i.e., $K_{c1} - K_{c2} = K_{c3} = K_{c4} = 1$), (f) frequency should be closely spaced. Unfortunately, the observed three transitions (McGuire et al. 2016) did not fulfill the above criterion. Thus, we are unable to predict the kinetic temperature from the line ratio method here. Alternatively, here, we have focused on the transitions of PrO which might be observed in the hot core region and identified some of the transitions which might be useful to find out the physical properties of the perceived source. In Table 9, we already have selected some transitions based on the obtained intensity and avoiding blending with possible interstellar species. Among them, we find out some transitions for the measurement of the kinetic temperature. The advantage of plotting these line ratios are that these are less sensitive to the calibration errors and both the lines would have been equally affected. It is worthy to calculate several transition ratios to avoid the discrepancy on measuring the kinetic temperature. We have found out following line pairs for the measurement of the kinetic temperature: $7_{35}-6_{34}/7_{44}-6_{43}$ ($E_{7_{44}} = 25.98K$), $7_{35}-6_{34}/7_{43}-6_{42}$ ($E_{7_{43}} = 25.98K$), $8_{27}-7_{26}/8_{54}-7_{53}$ ($E_{8_{54}} = 35.89K$), $9_{28}-8_{27}/9_{72}-8_{71}$ ($E_{9_{72}} = 54.83K$), $9_{45}-8_{44}/9_{46}-8_{45}$ ($E_{9_{46}} = 36.32K$), $10_{19}-9_{18}/10_{46}-9_{45}$ ($E_{10_{46}} = 42.40K$), $10_{66}-10_{65}/11_{92}-10_{91}$ ($E_{11_{92}} = 85.53K$), $11_{66}-10_{65}/11_{92}-10_{91}$ ($E_{11_{92}} = 85.53K$), $11_{65}-10_{64}/11_{93}-10_{92}$ ($E_{11_{93}} = 85.53K$), $11_{65}-10_{64}/11_{92}-10_{91}$ ($E_{11_{92}} = 85.53K$), $11_{47}-10_{46}/11_{93}-10_{92}$ ($E_{11_{93}} = 85.53K$), $11_{47}-10_{46}/11_{93}-10_{92}$ ($E_{11_{93}} = 85.53K$), $11_{47}-10_{46}/11_{66}-10_{65}$ ($E_{11_{66}} = 60.28K$), $11_{47}-10_{46}/11_{65}-10_{64}$ ($E_{11_{65}} = 60.28K$). The line ratios of PrO mentioned here have the transitions from various K_a ladders (i.e., with the $K_a = 3, 4, 5, 6, 7, 8, 9$). It is obvious that around the low-temperature region, the ground state of the K_a ladders are well populated and lower K_a values would pile up earlier than that of the higher K_a values.

From Fig. 9, the ground state of $K_a = 3, 4, 5, 6, 7, 8$ and 9 ladder is $3_{31}, 4_{41}, 5_{51}, 6_{61}, 7_{71}, 8_{81}$ and 9_{91} respectively. The upstate energy of the each transitions considered here are all below 100 K. Let us first check under LTE approximation how these ratios can behave. At the high densities, LTE conditions are best suited. Therefore, the relative population occupying the ground states from the two K_a ladders should obey the Boltzmann equation at the kinetic temperature. Mangum & Wootten (1993) derived the following relation for the estimation of kinetic temperature from the obtained line ratio if both the transitions are optically thin:

$$T_K = [E(J, K') - E(J, K)] \left[\ln \left(\frac{S_{JK'} \int J(T_R(J, K) d\nu)}{S_{JK} \int J(T_R(J, K') d\nu)} \right) \right]^{-1}, \quad (3)$$

where, $E(J, K')$ is the upstate energy of the bottom transition, $E(J, K)$ is the upstate energy of the transition at the numerator, $S_{JK'}$ and S_{JK} are the transition line strengths of the two upstate involved in the transition ratio and $T_R(J, K')$, $T_R(J, K)$ are the obtained radiation temperatures. By using the above relation and using the line strengths from <https://www.cv.nrao.edu/php/splat/advanced.php>, we have computed the line ratio of the radiation temperature for the above transitions. Fig. 10 shows the variation of these line ratio with the different kinetic temperature. It is interesting to note that around the low temperature, this ratio is maximum and drastically reduced with the increasing temperature. After a certain temperature, it remains roughly invariant

(small decreasing slope) on the increase of the kinetic temperature. This feature would be better understood if we explain it in terms of the 1^{st} transition ratio, $7_{35} - 6_{34}/7_{44} - 6_{43}$ ($E_{7_{44}} = 25.98K$) (see first panel of Fig. A4). Around the low temperature ($T_K < 25.98 K$) the ground state of the $K_a = 3$ (i.e., 3_{31}) and $K_a = 4$ ladder (i.e., 4_{41}) are mostly populated. Since 6_{34} level is lying below the 6_{43} level, its population is comparatively higher at the low temperature. Similarly, 7_{35} level lies below the 7_{44} level implies that the population is higher in 7_{35} level. As we have increased the temperature, population at the ground state falls much faster. Since the upper and lower level of the transition at the denominator is at a relatively higher energy level than that of the upper and lower energy level of the transition at the top, population in the 6_{43} level falls much faster than 7_{44} level and show faster-increasing trend of $7_{44} - 6_{43}$ transition in comparison to the top transition. At $T_K > E_u$ the decreasing slope of the ratio changes and at $T_K \gg E_u$ it tends to become roughly invariant on the kinetic temperature. The expression provided in eqn. 3 is independent of the the number density of the cloud and thus providing the kinetic temperature at the LTE condition. Since, we have considered the hot core region, where, the H_2 density should be on the higher side (may vary in between $\sim 10^5 - 10^7 \text{ cm}^{-3}$) and temperature in between $100 - 200 K$, LTE condition is best suited. Since from various observations, we know the kinetic temperature of Sgr B2 (Bonfand et al. 2017), we may constrain the line ratio of PrO around this region. Our obtained line ratios from the LTE condition are presented in Table 10 at $T_K = 150 K$.

Since we already have prepared our approximated collisional rate file, we have again calculated these line ratios with the non-LTE calculation for a wide range of parameter space. In our calculations, we have varied the kinetic temperature from 5 to 160 K and kept the column density of PrO constant at 10^{13} cm^{-2} . We also have considered the column density as high as $1.74 \times 10^{16} \text{ cm}^{-2}$ (obtained from our two-phase model presented in Fig. 4 and column density is obtained by assuming a H_2 column density of 10^{24} cm^{-2}) to see the effect on the calculated ratio but did not find any drastic difference. In Fig. A4, we have shown the line ratios which might be useful to precisely trace the temperature of the region where these lines would be observed. In the top of the panel, we have mentioned the upstate energy of four energy states which were involved in the transition ratio. In Table 10, we have also noted down our line ratios obtained from the non-LTE calculations with $n_H = 10^7 \text{ cm}^{-3}$ and $T_{ex} = 150 K$. It should be noted that the line ratios obtained from the LTE calculation are uncertain by $< 30\%$ (Mangum & Wootten 1993) and we have adopted random approximation for the consideration of our collisional data file. Despite this fact, we have obtained an excellent agreement between the LTE consideration and non-LTE calculation (Table 10).

5.3.2. Spatial density measurements:

Measurement of the spatial density is more critical than the measurement of the kinetic temperature. Based on the study by Mangum & Wootten (1993), spatial density could be measured by measuring a specific line ratio. Mangum & Wootten (1993) used the line ratio of various H_2CO transitions for

the measurement of the spatial density. Here, we have applied a similar technique to find out the line ratio for some of the observable transitions of PrO in the hot core region like Sgr B2(LMH). We have used the following criterion for the selection of the transition ratios: (a) $\Delta J = 1$ (i.e., $J_1 - J_2 = J_3 - J_4 = 1$), (b) $J_1 \neq J_3$ and $J_2 \neq J_4$, (c) $\Delta K_a = 0$ (i.e., $K_{a1} - K_{a2} = K_{a3} - K_{a4} = 0$), (d) $K_{a1} = K_{a2} = K_{a3} = K_{a4}$, (e) $\Delta K_c = 1$ (i.e., $K_{c1} - K_{c2} = K_{c3} - K_{c4} = 1$), (f) frequency should be closely spaced. Very rarely the above criteria are satisfied, and sometimes the frequency lies very far away, and thus absolute calibration of each transition is required. The observed three transitions (McGuire et al. 2016) are not satisfying the above criterion. We also did not find any other transitions which can satisfy the above criterion around the region (dark cloud condition) where these three transitions were observed. Thus, we have selected some more transitions ($7_{44} - 6_{43}/9_{46} - 8_{45}$, $7_{44} - 6_{43}/9_{45} - 8_{44}$, $7_{44} - 6_{42}/9_{46} - 8_{45}$, $7_{43} - 6_{42}/9_{45} - 8_{44}$, $8_{27} - 7_{26}/9_{28} - 8_{27}$) from the LTE model of the hot core region (Table 9) which can fulfill the above criterion and suitable for the observation in the hot core region. To constrain a limit on the number density, in Fig. A5, we have shown the line ratios of the PrO transitions for $T_{ex} = 150$ K. Here, the parameter space is based on the column density of PrO and the H_2 number density of the medium. Column density have been varied in between $10^{13} \text{ cm}^{-2} - 10^{16} \text{ cm}^{-2}$ and H_2 number density of the medium has been varied in between $10^4 - 10^7 \text{ cm}^{-3}$. The density and temperature of the Sgr B2 (LMH) region were well studied, and it would be assumed that the H_2 density may vary in between $10^6 - 10^7 \text{ cm}^{-3}$ and kinetic temperature may vary in between $100 - 150$ K. Assuming the predicted upper limit of the PrO column density of $6.7 \times 10^{14} \text{ cm}^{-2}$ from Cunningham et al. (2007), we have the line ratio of 0.55, 0.57, 0.57, 0.59 and 0.8 for the above 5 transitions respectively in the Sgr B2(LMH).

6. Conclusions

Presence of chiral species in the ISM been recently confirmed by McGuire et al. (2016). Observation of more chiral species and identification of their chirality may provide some lights on the homochirality of various pre-biotic species. In this paper, we have studied the chemical evolution of PrO under various physical conditions and find out the line parameters of its transitions which are relevant to constrain the physical properties of the source. The major conclusions are the following:

- A complete reaction network for the formation of PrO was prepared. This pathway is implemented in our gas-grain chemical model to find out its chemical evolution. To understand the formation of PrO in the cold environment as observed by (McGuire et al. 2016), we considered a static cloud model, and for the formation of PrO in the hot core region, we considered a two-phase model (static isothermal phase followed by a warm-up phase). We found that the reaction between C_3H_6 and $O(^3P)$ with an activation barrier of 40 K is the dominant means for the formation of PrO in the ice phase. This ice phase PrO desorbed to the gas phase by various means which could be observed by their rotational transitions. We also considered the formation of PrO by $O(^1D)$ but we in absence of this we also have significant PrO production due to the consideration of lower activation barrier for the reaction between C_3H_6 and $O(^3P)$.

Table 9. LTE line parameters of the various transitions of PrO using ALMA.

Transition ($J_{Ka'kc'} - J_{Ka''kc''}$)	Frequency (MHz)	E_{up} (K)	A_{ij} (s^{-1})	Tau	Tex (K)	Intensity (K)
16 2 15 - 16 1 16	85166.334	83.96	2.4E-06	1.30E-02	150	0.58
7 1 7 - 6 1 6	85484.159	17.01	3.0E-06	1.13E-02	150	0.51
17 4 14 - 17 3 15	85856.007	102.12	5.5E-06	2.73E-02	150	1.23
4 2 2 - 3 1 3	88348.483 ^a	8.33	3.8E-06	8.63E-03	150	0.39
7 3 5 - 6 3 4	88654.935	22.06	2.8E-06	9.49E-03	150	0.43
7 4 4 - 6 4 3	88599.017	25.98	2.3E-06	7.62E-03	150	0.35
7 4 3 - 6 4 2	88601.917	25.98	2.3E-06	7.62E-03	150	0.35
7 1 6 - 6 1 5	90475.090	17.98	3.5E-06	1.19E-02	150	0.55
17 2 16 - 17 1 17	90723.178	94.08	2.8E-06	1.30E-02	150	0.65
7 1 7 - 6 0 6	91337.880 ^{a,b}	17.01	8.0E-06	2.65E-02	150	1.24
8 0 8 - 7 1 7	94045.665 ^a	21.52	8.7E-06	3.00E-02	150	1.43
3 3 1 - 2 2 0	96421.008 ^{a,b}	8.70	1.0E-05	1.52E-02	150	0.73
18 5 13 - 18 4 14	97912.135	118.10	8.4E-06	3.04E-02	150	1.49
8 0 8 - 7 0 7	98662.010	21.52	4.7E-06	1.47E-02	150	0.72
8 2 7 - 7 2 6	100647.469	24.03	4.7E-06	1.40E-02	150	0.70
8 1 8 - 7 0 7	102188.761 ^a	21.69	1.2E-06	3.41E-02	150	1.70
5 2 3 - 4 1 4	103094.044	11.39	4.9E-06	9.71E-03	150	0.49
14 5 9 - 14 4 10	103204.976	77.85	8.9E-06	2.99E-02	150	1.51
6 2 5 - 5 1 4	105436.485 ^a	14.97	7.2E-06	1.57E-02	150	0.81
9 0 9 - 8 1 8	107006.105 ^{a,b}	26.82	1.4E-05	3.93E-02	150	2.01
4 3 2 - 3 2 1	108983.168 ^a	11.12	1.2E-05	1.75E-02	150	0.91
4 3 1 - 3 2 2	109160.580 ^a	11.12	1.2E-05	1.74E-02	150	0.91
9 2 8 - 8 2 7	113085.512	29.46	6.8E-06	1.73E-02	150	0.91
9 1 9 - 8 0 8	113153.015 ^{a,b}	26.95	1.7E-06	4.26E-02	150	2.24
9 7 2 - 8 7 1	113828.145	54.83	2.9E-06	6.12E-03	150	0.32
9 4 6 - 8 4 5	114012.677	36.32	5.9E-06	1.41E-02	150	0.74
9 4 5 - 8 4 4	114031.614	36.32	5.9E-06	1.41E-02	150	0.74
17 6 11 - 17 5 12	126748.398	113.19	1.6E-05	3.50E-02	150	1.94
10 4 6 - 9 4 5	126783.156	42.40	8.6E-06	1.75E-02	150	0.97
14 6 8 - 14 5 9	127852.183	83.99	1.6E-05	3.30E-02	150	1.83
15 6 10 - 15 5 11	127659.038	93.11	1.6E-05	3.41E-02	150	1.89
16 6 11 - 16 5 12	127377.638	102.84	1.6E-05	3.48E-02	150	1.93
9 6 3 - 9 5 4	128562.724	47.53	1.2E-05	2.10E-02	150	1.17
10 6 5 - 10 5 6	128487.914	53.60	1.3E-05	2.44E-02	150	1.36
13 6 7 - 13 5 8	128075.357	75.48	1.5E-05	3.16E-02	150	1.75
13 6 8 - 13 5 9	128097.570	75.48	1.5E-05	3.16E-02	150	1.75
12 6 6 - 12 5 7	128249.483	67.58	1.5E-05	2.96E-02	150	1.65
10 1 9 - 9 1 8	128225.980	34.64	1.0E-05	2.19E-02	150	1.22
12 6 7 - 12 5 8	128259.465	67.58	1.5E-05	2.96E-02	150	1.65
10 6 4 - 10 5 5	128486.347	53.60	1.3E-05	2.44E-02	150	1.36
11 0 11 - 10 1 10	132290.717	39.14	2.8E-05	5.94E-02	150	3.32
6 3 4 - 5 2 3	133619.742	17.81	1.7E-05	2.26E-02	150	1.28
11 9 2 - 10 9 1	139104.681	85.53	4.5E-06	6.26E-03	150	0.36
11 9 3 - 10 9 2	139104.681	85.53	4.5E-06	6.26E-03	150	0.36
11 8 3 - 10 8 2	139131.647	75.99	6.4E-06	9.50E-03	150	0.54
11 8 4 - 10 8 3	139131.647	75.99	6.4E-06	9.50E-03	150	0.54
11 6 6 - 10 6 5	139230.454	60.28	9.5E-06	1.58E-02	150	0.91
11 6 5 - 10 6 4	139230.502	60.28	9.5E-06	1.58E-02	150	0.91
11 4 7 - 10 4 6	139567.307	49.10	1.2E-05	2.10E-02	150	1.21
16 7 10 - 16 6 11	151281.705	110.10	2.5E-05	3.69E-02	150	2.16
14 7 8 - 14 6 9	151616.943	91.27	2.4E-05	3.45E-02	150	2.02
13 7 7 - 13 6 8	151740.138	82.76	2.3E-05	3.25E-02	150	1.91
8 7 1 - 8 6 2	152054.582	49.36	1.2E-05	1.36E-02	150	0.80
8 7 2 - 8 6 3	152054.583	49.36	1.2E-05	1.36E-02	150	0.80
12 5 8 - 11 5 7	152058.401	61.42	1.5E-05	2.20E-02	150	1.29
12 5 7 - 11 5 6	152064.369	61.42	1.5E-05	2.20E-02	150	1.90
11 2 10 - 10 1 9	155300.752	42.09	2.5E-04	3.83E-02	150	2.26
13 1 13 - 12 0 12	158512.466	53.75	5.1E-04	8.07E-02	150	4.74

^a Attempted in Orion KL by Cunningham et al. (2007)^b Attempted in Sgr B2 by Cunningham et al. (2007)

ALMA Band 3 = 84-116 GHz

ALMA Band 4 = 125-163 GHz

Table 10. Estimated line ratio of PrO for the measurement of Kinetic temperature at 150K from LTE and non-LTE.

Line ratio (upstate energy in K)	LTE results	non-LTE results
$7_{35} - 6_{34} / 7_{44} - 6_{43} (E_{7_{44}} = 25.98)$	1.24	1.25
$7_{35} - 6_{34} / 7_{43} - 6_{42} (E_{7_{43}} = 25.98)$	1.24	1.25
$8_{27} - 7_{26} / 8_{54} - 7_{53} (E_{8_{54}} = 35.89)$	1.66	1.65
$9_{28} - 8_{27} / 9_{72} - 8_{71} (E_{9_{72}} = 54.83)$	2.84	2.78
$9_{45} - 8_{44} / 9_{46} - 8_{45} (E_{9_{46}} = 36.32)$	0.99	1.00
$10_{19} - 9_{18} / 10_{46} - 9_{45} (E_{10_{46}} = 42.40)$	1.23	1.25
$10_{66} - 10_{65} / 11_{92} - 10_{91} (E_{11_{92}} = 85.53)$	2.51	2.53
$11_{66} - 10_{65} / 11_{92} - 10_{91} (E_{11_{92}} = 85.53)$	2.51	2.53
$11_{65} - 10_{64} / 11_{93} - 10_{92} (E_{11_{93}} = 85.53)$	2.51	2.53
$11_{65} - 10_{64} / 11_{92} - 10_{91} (E_{11_{92}} = 85.53)$	2.51	2.53
$11_{47} - 10_{46} / 11_{92} - 10_{91} (E_{11_{93}} = 85.53)$	3.35	3.32
$11_{47} - 10_{46} / 11_{93} - 10_{92} (E_{11_{93}} = 85.53)$	3.35	3.32
$11_{47} - 10_{46} / 11_{66} - 10_{65} (E_{11_{66}} = 60.28)$	1.33	1.31
$11_{47} - 10_{46} / 11_{65} - 10_{64} (E_{11_{65}} = 60.28)$	1.33	1.31

- We computed various vibrational transitions of PrO along with its protonated form which might be observable with the forthcoming JWST facility.

- To constrain the physical properties of the cloud, we carried out non-LTE modeling (by considering approximated collisional data file) for the most probable transitions identified by the LTE calculations by considering a wide range of parameter space (spanned by the H₂ density range

of $\sim 10^3 - 10^7 \text{ cm}^{-3}$ of the collisional partner and the kinetic temperature range of $\sim 5 - 35 \text{ K}$. We found that the observed three transitions at 12.07243 GHz ($1_{10} - 1_{01}$), 12.83734 GHz ($2_{11} - 2_{02}$) and 14.04776 GHz ($3_{12} - 3_{03}$) showed absorption features around the high H_2 density ($10^4 - 10^7 \text{ cm}^{-3}$) and low temperature ($< 10 \text{ K}$) region. Additionally, we found three more transitions (at 15.78, 18.10 and 23.975 GHz) which might be observed in absorption around the same region where the three transitions were identified by McGuire et al. (2016).

- We identified the line parameters suitable for the hot core observation of PrO. Potentially observable transitions lying in the ALMA Band 3 and Band 4 are pointed out which would be used for the future observations.

- Various line ratios were directly found to be linked with the kinetic temperature and spatial density distribution. Thus from observation, one can extract the physical properties of the star-forming region by comparing their observation with our proposed parameters.

Our result depends on a very simple-minded cloud model which has no rotation and also the evolution was done until an estimated time. Thus the estimation of the parameters mentioned above could slightly depend on the evolution time inside the cloud. These aspects would be further explored in the future.

Acknowledgements. This research was possible in part due to a Grant-In-Aid from the Higher Education Department of the Government of West Bengal. AD is grateful to ISRO Respond project (Grant No. ISRO/RES/2/402/16-17) PG acknowledge CSIR extended SRF fellowship (Grant No. 09/904 (0013) 2018 EMR-I). We want to acknowledge the reviewer for the numerous suggestion to improve the paper.

References

- Abplanalp, M. J., Förstel, M., & Kaiser, R. I. 2016, CPL, 644, 79
- Adams F.C., Lada C.J. & Shu F.H., 1987, ApJ, 312, 788.
- Agúndez, M., & Wakelam, V., 2013, Chem. Rev., 113, 8710
- Atkinson, R., & Cvetanov, R. J. 1972, JChPh., 56, 432.
- Atkinson, R., & Pitts, J. N. 1974, Chem. Phys. Lett., 27, 467.
- Bailey J., Chrysostomou A., Hough J.H., Gledhill T.M., McCall A., Clark S., Menard F. & Tamura M. 1998, Sci, 281, 672.
- Bacmann A., Taquet V., Faure A., Kahane C. & Ceccarelli C., 2012, A&A, 541, L12.
- Becke, A.D., 1988, Phys. Rev. A, 38(6), 3098
- Bergner, J. B., Öberg, K. I., & Rajappan, M., 2017, ApJ, 845, 29
- Bergantini, A., Abplanalp, M.J., Pokhilko, P., et al. 2018, ApJ, 860, 108
- Breslow, R & Cheng, Z-L 2009, PNAS, 106, 9144
- Breslow R, Levine M, & Cheng ZL., 2010, Orig Life Evol Biosph, 40, 11
- Busemann H., Young A. F., O D. Alexander C. M., Hoppe P., Mukhopadhyay S. & Nittler L. R., 2006, Sci, 312, 727.
- Bonfand, M., Belloche, A., Menten, K. M., Garrod, R.T., Müller, H. S. P, 2017, A&A, 604, 60
- Cohen, J., 1995, Sci, 267, 1265.
- Creswell, R.A., & Schwendeman, R.H. 1977, Journal of Molecular Spectroscopy, 64, 295.
- Cunningham, M.R., P.A., Godfrey, P.D., et al., 2007, MNRAS, 376, 1201.
- Chakrabarti, S., & Chakrabarti, S.K. 2000a, A&A, 354, L6
- Chakrabarti, S.K., & Chakrabarti, S. 2000b, InJPh, 74B, 97
- Chakrabarti, S.K., Das, A., Acharyya, K., & Chakrabarti, S. 2006a, A&A, 457, 167
- Chakrabarti, S.K., Das, A., Acharyya, K., & Chakrabarti, S. 2006b, BASI, 34, 299
- Chakrabarti, S.K., Majumdar, L., Das, A., & Chakrabarti, S. 2015, Ap&SS, 357, 90

- Chyba, C. F., Thomas, P. J., Brookshaw, L., & Sagan, K, 1990, *Sci*, 249, 366
- Das, A., Sil, M., Gorai, P., Chakrabarti, S.K., Loison, J.C., 2018, *ApJS*, 237, 9
- Das, A., Chakrabarti, S.K., Acharyya K., & Chakrabarti, S. 2008a, *NewA*, 13, 457
- Das, A., Acharyya, K., Chakrabarti, S. & Chakrabarti, S. K., 2008b, *A&A*, 486, 209
- Das, A., Acharyya, K. & Chakrabarti, S. K., 2010, *MNRAS* 409, 789
- Das, A., & Chakrabarti, S.K. 2011, *MNRAS*, 418, 545
- Das, A., Majumdar, L., Chakrabarti, S.K., & Chakrabarti, S. 2013a, *NewA*, 23, 118
- Das, A., Majumdar, L., Chakrabarti, S.K., Saha, R., & Chakrabarti, S. 2013b, *MNRAS*, 433, 3152
- Das, A., Majumdar, L., Chakrabarti, S.K., & Sahu, D. 2015a, *NewA*, 35, 53
- Das, A., Majumdar, L., Sahu, D., Gorai, P., Sivaraman, B., & Chakrabarti, S.K. 2015b, *ApJ*, 808, 21
- Das, A., Sahu, D., Majumdar, L., & Chakrabarti, S.K. 2016, *MNRAS*, 455, 540
- DeBoer, G.D. & Dodd, J.A., 2007, *JPhCh. A*, 111, 12977.
- Dubnikova, F. & Lifshitz, A. 2000, *JPhCh*, 104, 4489.
- Dickens, J.E, Irvine, W.M., Ohishi, M., et al., 1997, *ApJ*, 489, 753.
- Engel, M. H., & Macko, S. A., 1997, *Nature*, 389, 265.
- Engel, M. H. & Nagy, B. 1982, *Nature*, 296, 837
- Frisch, M. J., Trucks, G. W., Schlegel, H. B., et al., 2015, *Gaussian 09*, Revision A.02. (Wallingford, CT: Gaussian Inc.)
- Gontrani, L., Nunziante C.S., Stranges, S., Bencivenni, L., & Pieretti, A. 2014, *AcSpe*, 120, 558.
- Gorai, P., Das, A., Das, A., Sivaraman, B., Etim, E.E., & Chakrabarti, S.K. 2017a, *ApJ*, 836, 70
- Gorai, P., Das, A., Majumdar, L., Chakrabarti, S.K., Sivaraman, B., & Herbst, E. 2017b, *MolAs*, 6, 36
- Gupta, V.R., Tandon, P., Rawat, P., Singh, R.N., Singh, A., 2011. *A&A* 528, A129.
- Hershbach, D.R. & Swalen, J.D., 1958, *JChPh*, 29, 4.
- Herbst E., Klemperer W. 1973, *ApJ*, 185, 505
- Herbst E., van Dishoeck E.F., 2009, *ARA&A*, 47, 427.
- Herbs.E., Roueff. E. & Talbi. D, 2010, *Molecular Physics*, 108, 2171.
- Hocuk, S., Szűcs, L., Caselli, P., Cazaux, S., Spaans, M. and Esplugues, G.B., 2017, *A&A*, 604, A58.
- Hunter, E. P., & Lias, S. G. 1998, *JPCRD*, 27, 413
- Garrod, R.T., 2013, *ApJ*, 765, 60.
- Garrod, R. T., & Herbst, E. 2006, *A&A*, 457, 927.
- Garrod, R. T., Wakelam, V., & Herbst, E. 2007, *A&A*, 467, 1103.
- Gredel, R., Lepp, S., Dalgarno, A., & Herbst, E., 1989, *ApJ*, 347, 289.
- Hasegawa, T., Herbst, E., & Leung, C.M., 1992, *ApJ*, 82, 167.
- Hartogh, P., Lis, D. C., Bockelée-Morvan, D et al., 2011, *Nature*, 478, 218
- He, J., Shi, J., Hopkins, T., Vidal, G., & Kaufman, M. J., 2015, *ApJ*, 801, 120
- Herbst, E., Klemperer, W., 1973, *ApJ*, 185, 505.
- Herbst, E., 2006, in *Springer Handbook of Atomic, Mol. & Opt. Phys.*, ed. G.W.F. Drake (New York: Springer), 561
- Hogerheijde & van der Tak. 2000, *A&A* 362, 697.
- Hollis, J.M., Jewell, P.R., Remijan, A.J., Lovas, F.J., 2007, *ApJ*, 660, L126
- Hickson, K.M., Wakelam, V., Loison, J-C., 2016, *MolAp*, 3-4, 1-9.
- Hincelin, U., Wakelam, V., Hersant, F., Guilloteau, S., Loison, J-C. et al., 2011, *A&A*, 530, A61.
- Holtom P.D., Bennett C.J., Osamura Y., Mason N.J., Kaiser R.I. 2005, *ApJ*, 626, 940.
- Hunt-Cunningham M.R., Jones P.A. 2004, *IAUS*, 213, 159.
- Hudon, R.L., Loeffler, M.J., Yocum. K.M. 2017, *ApJ*, 835, 225.
- Knyazev, V.D., Arutyunov, V.S., & Vedenev, V.I. 1992, *Int. J. Chem. Kinet.* 24, 545.
- Lauck, T., Karssemeijer, L., Shulenberger, K., et al. 2015, *ApJ*, 801, 118
- Leonori, F., Balucani, N., Nevrlý, V., Bergeat, A., Falcinelli, S., Vanuzzo, G., Casavecchia, P., 2015, *JPCC*, 119, 26, 14632.
- Lee H. H., Herbst E., Pineau des Forets G., Roueff E., Le Bourlot J., 1996, *A&A*, 311, 690
- Lee, C., Yang, W., & Parr, R.G., 1988, *Phys. Rev. B*, 58, 785

- Lin, Z., Talbi, D., Roueff, E., Eric Herbst, E. et al. 2013, *ApJ*, 765, 80.
- Lowe, M.A., Alper, J.S., Kawiecki, R., Stephens, P.J. 1986, *JphCh*, 90, 41, 50.
- Majumdar, L., Das, A., Chakrabarti, S.K., & Chakrabarti, S. 2012, *RAA*, 12, 1613
- Majumdar, L., Das, A., Chakrabarti, S.K., & Chakrabarti, S. 2013, *NewA*, 20, 15
- Majumdar, L., Das, A., & Chakrabarti, S.K. 2014a, *A&A*, 562, A56
- Majumdar, L., Das, A., & Chakrabarti, S.K. 2014b, *ApJ*, 782, 73
- Mangum, J.G. & Wootten, A., 1993, *ApJSS*, 89, 123.
- Marcelino, N., Cernicharo, J., Agúndez, M., et al. 2007, *ApJ*, 665, L127.
- McElroy, D., Walsh, C., Markwick, A.J., Cordiner, M.A., Smith, K., & Millar, T.J. 2013, *A&A*, 550, A36.
- McGuire, B.A., Carroll, P.B., Loomis, R.A., et al. 2016, *Science*, 352, 1449.
- Nuevo, M., Materese, C.K., & Sandford, S.A. 2014, *ApJ*, 793, 125.
- Öberg, K.I., Garrod R.T., van Dishoeck E.F., Linnartz H. 2009, *A&A*, 504, 891.
- Occhiogrosso, A., Viti, S., Ward, M.D., & Price, S.D. 2012, *MNRAS*, 427, 2450.
- Polavarapu, P.L., Hess Jr. B.A., & Schaad, L.J. 1985, *The Journal of Chemical Physics* 82, 1705.
- Puzzarini, C., Ali, A., Biczysko, M., & Barone, V. 2014, *ApJ*, 792, 118
- Rabli, D. & Flower, D.R. 2010, *MNRAS* 406, 95
- Raymond, S. N., Quinn, T.R., & Lunine, J. I., 2004, *Icarus*, 168 (1), 1-17
- Ruaud, M., Wakelam, V., Hersant, F. 2016, *MNRAS*, 459, 3756.
- Schiwietz, G. & Grande, P.L., 2011, *Physical Review A*, 84, 052703
- Schöier, F.L., van der Tak, F.F.S., van Dishoeck E.F. & Black, J.H. 2005, *A&A* 432, 369-379
- Sil, M., Gorai, P., Das, A., Bhat, B. et al. 2017, *ApJ*, 853, 2.
- Shu, F., 1977, *ApJ* 214, 488.
- Stuhl, F., & Niki, H. 1971, *J. Chem. Phys.*, 55, 3954.
- Swalen, J.D.; Herschbach, D.R. 1957, *J. Chem. Phys.*, 27, 100.
- Su, T., & Chesnavich, W.J., 1982, *J. Chem. Phys.*, 76, 5183
- Vasyunin, A.I., & Herbst, E. 2013, *ApJ*, 769, 34.
- Van der Tak, F.F.S., 2011, *Proceedings IAU Symposium No. 280*, 2011, Editors: Cernicharo, J. & Bachiller, R.
- Van der Tak, F.F.S., Black, J.H., Schöier, F.L., Jansen, D.J., van Dishoeck, E.F. 2007, *A&A* 468, 627.
- Wakelam, V., Smith, I.W.M. Smith, & Herbst, E., et al., 2010, *Space Sci. Rev.*, 156, 1, 13
- Ward, M.D., & Price, S.P. 2011, *ApJ*, 741, 2011.
- Woodall, J., Agnèz, M., Markwick-Kemper, A.J., Millar, T.J., 2007, *A&A*, 466, 1197
- Woon, D.E., 2002, *ApJ*, 571, L177
- Woon, D.E., & Herbst, E., 2009, *ApJSS*, 185, 273

Appendix A: Additional Figures

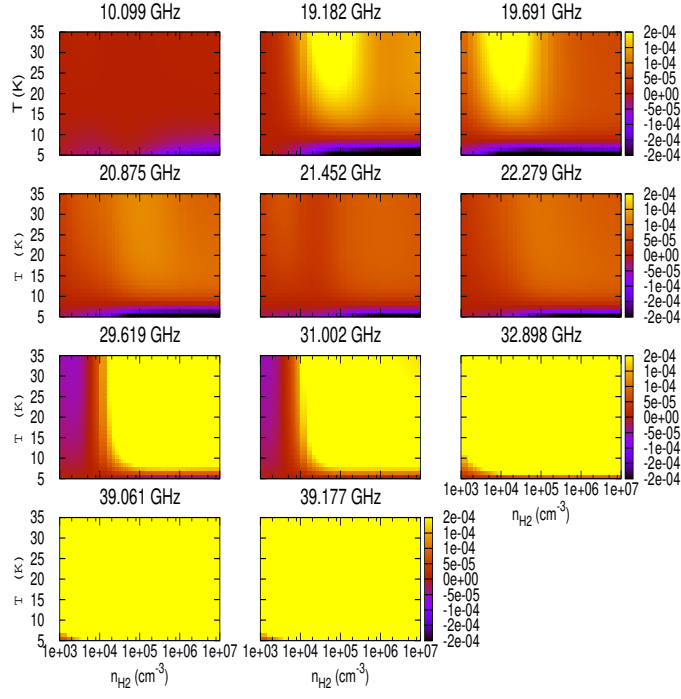


Fig. A1. Parameter space for the radiation temperature of the 11 observed propenal transitions with non-LTE condition.

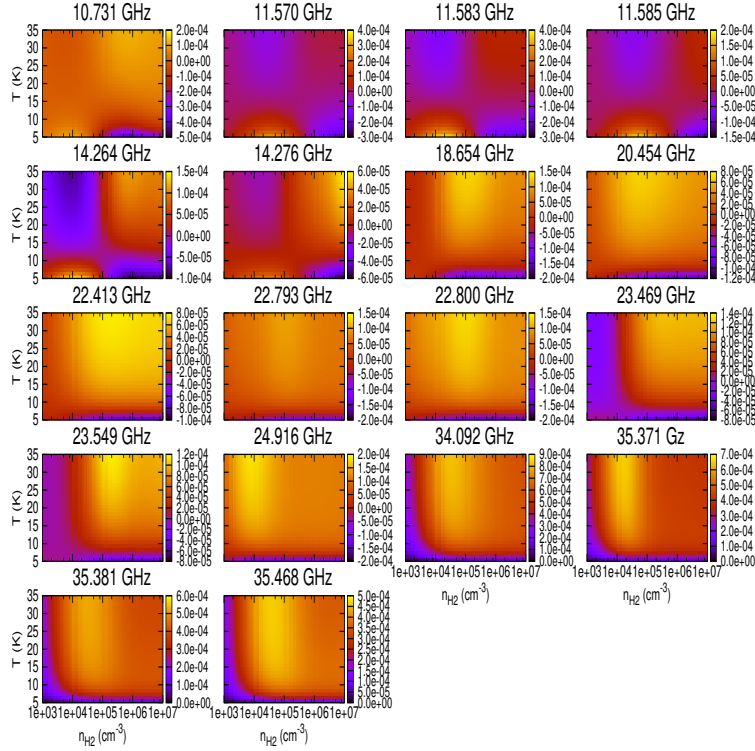


Fig. A2. Parameter space for the radiation temperature of the 18 observed acetone transitions with non-LTE condition.

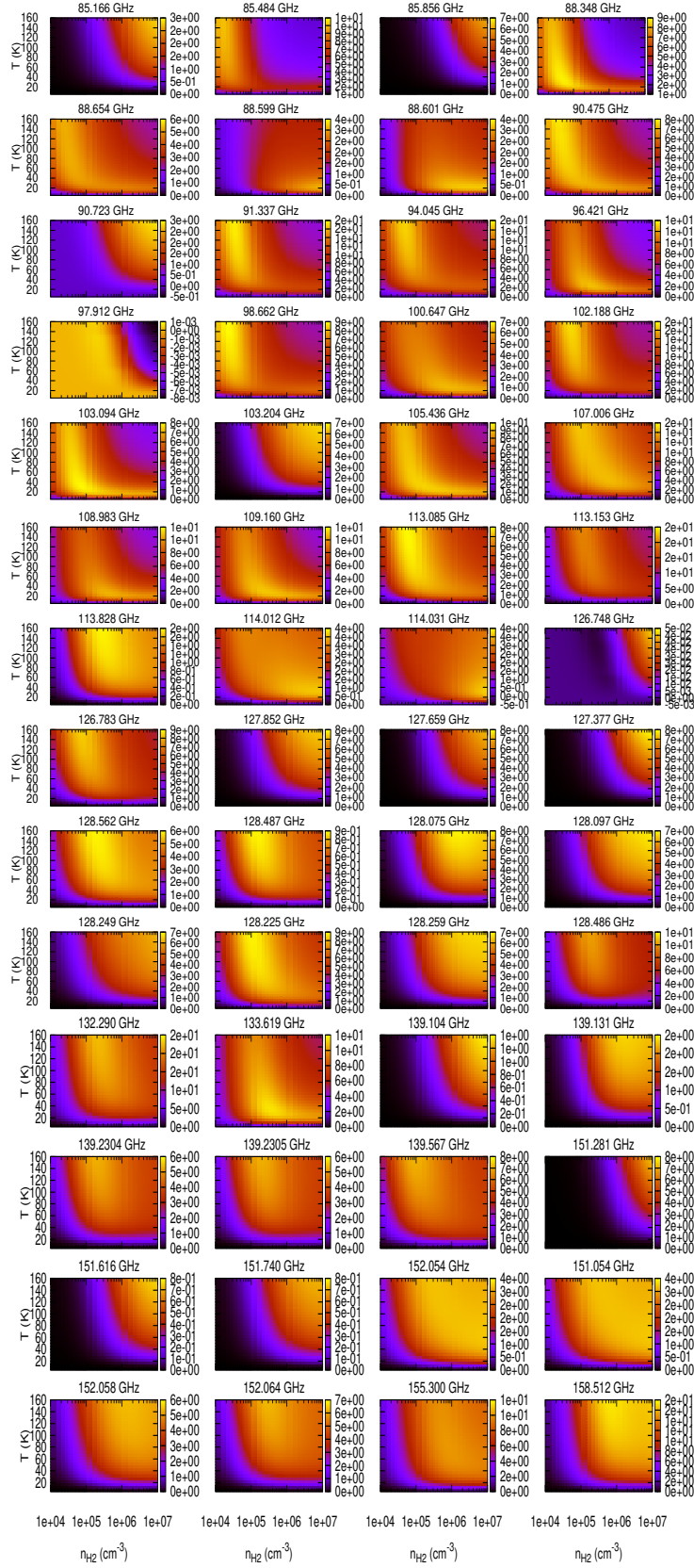


Fig. A3. Parameter space of the radiation temperature for the probable PrO transitions in the hot core region.

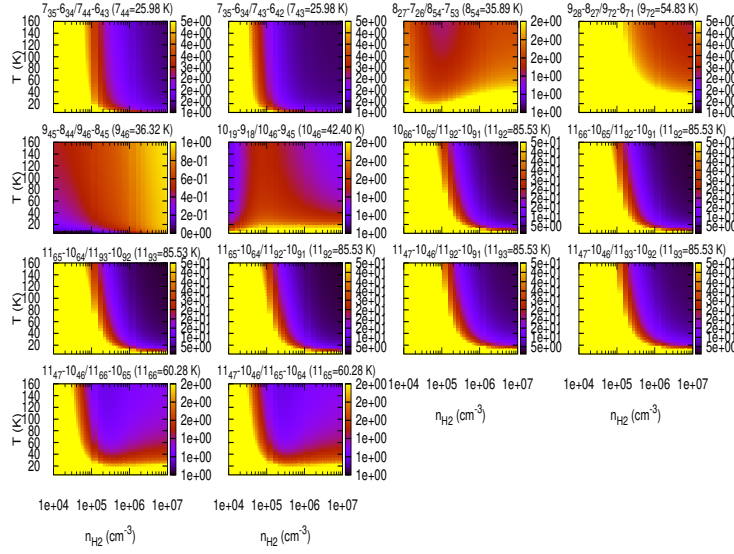


Fig. A4. Variation of the line ratios (useful for the kinetic temperature measurement) for a wide range of parameter space (number density and kinetic temperature).

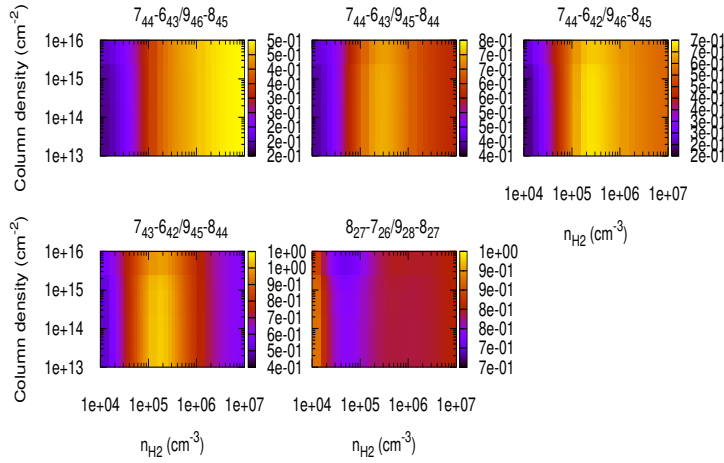


Fig. A5. Variation of line ratios (useful for the measurement of the spatial density) for a wide range of parameter space (column density and number density).